Far-infrared and dust properties of present-day galaxies in the EAGLE simulations

Peter Camps,[1]★ James W. Trayford,[2] Maarten Baes,[1] Tom Theuns,[2] Matthieu Schaller[2] and Joop Schaye[3]

[1]*Sterrenkundig Observatorium, Universiteit Gent, Krijgslaan 281, B-9000 Gent, Belgium*

[2]*Institute for Computational Cosmology, Department of Physics, University of Durham, South Road, Durham DH1 3LE, UK*

[3]*Leiden Observatory, Leiden University, PO Box 9513, NL-2300 RA Leiden, the Netherlands*

ABSTRACT

The Evolution and Assembly of GaLaxies and their Environments (EAGLE) cosmological simulations reproduce the observed galaxy stellar mass function and many galaxy properties. In this work, we study the dust-related properties of present-day EAGLE galaxies through mock observations in the far-infrared and submm wavelength ranges obtained with the 3D dust radiative transfer code SKIRT. To prepare an EAGLE galaxy for radiative transfer processing, we derive a diffuse dust distribution from the gas particles and we re-sample the star-forming gas particles and the youngest star particles into star-forming regions that are assigned dedicated emission templates. We select a set of redshift-zero EAGLE galaxies that matches the *K*-band luminosity distribution of the galaxies in the *Herschel* Reference Survey (HRS), a volume-limited sample of about 300 normal galaxies in the Local Universe. We find overall agreement of the EAGLE dust scaling relations with those observed in the HRS, such as the dust-to-stellar mass ratio versus stellar mass and versus NUV–*r* colour relations. A discrepancy in the f_{250}/f_{350} versus f_{350}/f_{500} submm colour–colour relation implies that part of the simulated dust is insufficiently heated, likely because of limitations in our sub-grid model for star-forming regions. We also investigate the effect of adjusting the metal-to-dust ratio and the covering factor of the photodissociation regions surrounding the star-forming cores. We are able to constrain the important dust-related parameters in our method, informing the calculation of dust attenuation for EAGLE galaxies in the UV and optical domain.

Key words: radiative transfer – methods: numerical – dust, extinction – galaxies: formation – infrared: ISM.

1 INTRODUCTION

Cosmological simulations are a valuable tool in the study of how galaxies form and evolve. Recently, hydrodynamical simulations of the formation of galaxies in cosmologically representative volumes have succeeded in reproducing many – but not all – observed properties of galaxies and of the intergalactic medium to unprecedented levels of agreement (e.g. Le Brun et al. 2014; Vogelsberger et al. 2014; Schaye et al. 2015). The mass resolution for baryonic matter in these simulations is on the order of 10^6 solar masses. Physical processes on unresolved scales (including star formation and stellar feedback) are handled through sub-grid prescriptions. Zoom-in simulations (e.g. Hopkins et al. 2014; Wang et al. 2015; McKinnon, Torrey & Vogelsberger 2016; Sawala et al. 2016) offer

a better resolution, however, they still use similar sub-grid prescriptions. Inevitably these limitations lead to uncertainties in some of the simulation predictions.

By comparing simulation results and observations we hope to examine the empirical scaling laws, deduce improved sub-grid prescriptions, and eventually, to further our understanding of the underlying physical processes. Because properties of real galaxies are derived from observed quantities (i.e. fluxes), they may be subject to unknown systematic biases. Making mock observations of simulated galaxies enables direct comparison to observational data, and helps to characterize the systematics involved in the transformation between intrinsic and observed quantities (see e.g. Guidi, Scannapieco & Walcher 2015; Hayward & Smith 2015).

Extinction by dust grains residing in the interstellar medium (ISM) can substantially influence the flux detected from a galaxy in the UV and optical wavelength ranges. It is very hard to estimate the dust mass in a galaxy based solely on the information at

★ E-mail: Peter.Camps@ugent.be

these wavelengths, and thus it is difficult to account accurately for the dust obscuration effect (e.g. Disney, Davies & Phillipps 1989; Byun, Freeman & Kylafis 1994). To alleviate this limitation, one can turn to the far-infrared (FIR) to submm wavelength range. In this window, the continuum spectra of star-forming galaxies are dominated by thermal emission from dust grains that reprocess the UV/optical radiation, providing an independent and more direct measurement of the amount of dust in a galaxy. This additional information is especially useful for constraining the dust modelling of numerically simulated galaxies that have no explicit dust component. On the other hand, accurately predicting dust emission from a simulated galaxy requires solving a non-trivial 3D radiative transfer problem (see e.g. Whitney 2011; Steinacker, Baes & Gordon 2013).

Several authors have performed UV to submm radiative transfer modelling for up to a few dozen simulations of isolated galaxies or galaxy mergers (e.g. Jonsson, Groves & Cox 2010; Narayanan et al. 2010a,b; Scannapieco et al. 2010; Hayward et al. 2011, 2012, 2013, 2014; Robitaille et al. 2012; Domínguez-Tenreiro et al. 2014; Hayward & Smith 2015; Saftly et al. 2015). While Torrey et al. (2015) do produce mock images and SEDs for thousands of present-day galaxies in the cosmological simulation Illustris (Vogelsberger et al. 2014), they do not include dust emission, limiting the observables to UV, optical and near-infrared (NIR) wavelengths. In this work, we study the effects of dust in the full UV to submm wavelength range. We use simulated galaxies that were evolved as part of a cosmologically representative volume, and that are available in sufficiently large numbers to allow a statistically relevant confrontation with observations.

Specifically, we concentrate on the FIR and dust-related properties of the present-day galaxies produced by the Evolution and Assembly of GaLaxies and their Environments (EAGLE) simulations (Crain et al. 2015; Schaye et al. 2015). EAGLE is a suite of hydrodynamical simulations of the formation of galaxies in cosmologically representative volumes, with sub-grid models for radiative cooling, star formation, stellar mass loss, and feedback from stars and accreting black holes. The sub-grid physics recipes are calibrated to reproduce the present-day galaxy stellar mass function and galaxy sizes, and show good agreement with many observables not considered in the calibration, including present-day specific star formation rates (sSFRs), passive fractions, the Tully–Fisher relation (Schaye et al. 2015), and the neutral gas content (Bahé et al. 2016). The simulations also track the observed evolution of the galaxy stellar mass function out to redshift $z = 7$ (Furlong et al. 2015) and reproduce the observed optical colours for galaxies in the Local Universe (Trayford et al. 2015; Trayford et al., in preparation).

We use the *Herschel* Reference Survey (Boselli et al. 2010) (HRS), a volume-limited sample of about 300 'normal' galaxies in the Local Universe, as a reference for observed dust properties. We select a set of redshift-zero EAGLE galaxies that matches the *K*-band luminosity distribution of the HRS galaxies, and we use the 3D dust radiative transfer code SKIRT (Baes et al. 2011; Camps & Baes 2015) to calculate observable properties for these galaxies from UV to submm wavelengths. We compare the stellar mass, dust mass, and star formation rate (SFR) derived from our mock observations through standard tracers with the intrinsic EAGLE values, and we compare the EAGLE dust scaling relations with those observed for HRS galaxies presented by Boselli et al. (2012) and Cortese et al. (2012). Finally, we investigate the effect of varying dust-related parameters in our post-processing procedure. This allows us to constrain these parameters, thus informing the calculation of

dust attenuation for EAGLE galaxies in the UV and optical domain by Trayford et al. (in preparation).

In Section 2 we provide some background on the EAGLE simulations and the SKIRT radiative transfer code, and we describe how the EAGLE results were exported to and post-processed by SKIRT, with some details relayed to the appendices. In Section 3 we present and discuss the results of our analysis, and in Section 4 we summarize and conclude.

2 METHODS

2.1 The EAGLE simulations

The EAGLE project (Crain et al. 2015; Schaye et al. 2015) is comprised of a suite of smoothed particle hydrodynamics (SPH) simulations that follow the formation of galaxies and large-scale structure in cosmologically representative volumes of a standard Λ cold dark matter universe. EAGLE uses the hydrodynamics code GADGET (first described by Springel 2005), but employs an improved hydrodynamics scheme, referred to as ANARCHY, described by Schaye et al. (2015) and Schaller et al. (2015). The sub-grid models used in EAGLE are based on those developed for OWLS (Schaye et al. 2010). They are described in detail in Schaye et al. (2015) and summarized very briefly below.

Hydrogen reionization is modelled by turning on the time-dependent, spatially uniform UV/X-ray background from Haardt & Madau (2001) at redshift $z = 11.5$. Radiative cooling and photo-heating are implemented element by element following Wiersma, Schaye & Smith (2009a), including all 11 elements that they found to dominate the radiative rates. Star formation follows Schaye & Dalla Vecchia (2008), but with the metallicity-dependent density threshold of Schaye (2004). Stellar mass-loss and chemical enrichment is based on Wiersma et al. (2009b) and tracks the elements H, He, C, N, O, Ne, Mg, Si, and Fe individually, while fixed abundance ratios relative to Si are assumed for Ca and S. Energetic feedback from star formation uses a stochastic thermal feedback scheme following Dalla Vecchia & Schaye (2012), with a variable efficiency depending on local gas density and metallicity. A super-massive black hole seed is placed at the centre of every halo above a threshold mass (Springel, Di Matteo & Hernquist 2005) and is allowed to grow through gas accretion and mergers (Rosas-Guevara et al. 2015; Schaye et al. 2015). Feedback from these accreting black holes quenches star formation in massive galaxies, shapes the gas profiles in the inner parts of their host haloes, and regulates the growth of the black holes themselves.

A drawback for the purpose of this work is that the EAGLE simulations do not model the cold gas phase in the ISM (see section 4.3 of Schaye et al. 2015). To limit the pressure of star-forming gas particles, the EAGLE simulations impose a temperature floor, $T_{eos}(\rho)$, as a function of the local gas density, ρ, corresponding to the polytropic equation of state $\rho\, T_{eos} \propto P_{eos} \propto \rho^{4/3}$ (Schaye & Dalla Vecchia 2008). As a consequence, there are no resolved molecular clouds. Instead, the simulated ISM consists of smoothly distributed, warm gas. We address this issue to some extent by employing a separate sub-grid model for star-forming regions in our post-processing procedure (see Section 2.4.4), and by assigning dust to star-forming gas particles regardless of their imposed, unphysical temperature (see Section 2.4.3). It remains important, however, to keep this limitation in mind when interpreting our results.

To enable numerical convergence studies, the EAGLE suite includes simulations with varying spatial resolution and simulation volume. In this work, we use the redshift-zero snapshots of the

Table 1. We use the redshift-zero snapshots of the three EAGLE simulations listed in this table. We refer to them through the labels in the first column. The second column shows the corresponding full EAGLE simulation name as defined in tables 2 and 3 in Schaye et al. (2015). The remaining columns list the simulation's comoving box size, the initial number of baryonic particles, the initial baryonic particle mass, and the maximum proper gravitational softening length (i.e. at redshift zero).

Label	EAGLE name	L (cMpc)	N	$m_{\rm g}$ ($M_\odot$)	$\epsilon_{\rm prop}$ (kpc)
Ref100	Ref-L100N1504	100	1504^3	1.81×10^6	0.70
Recal25	Recal-L025N0752	25	752^3	2.26×10^5	0.35
Ref25	Ref-L025N0752	25	752^3	2.26×10^5	0.35

three EAGLE simulations listed in Table 1. The sub-grid prescriptions in the EAGLE reference simulation ('Ref100' in Table 1) are calibrated to reproduce the present-day galaxy stellar mass function. One of the higher resolution simulations ('Ref25' in Table 1) employs the same sub-grid parameter values, i.e. calibrated for the resolution of the Ref100 simulation. For the other simulation ('Recal25' in Table 1), the sub-grid prescriptions have been recalibrated to compensate for the effects of the increased numerical resolution. This approach allows investigating the 'weak' and 'strong' convergence properties of the simulations, as explained in Schaye et al. (2015).

The public data base presented by McAlpine et al. (2016) lists a wide range of properties for the galaxies in the EAGLE simulations, including intrinsic quantities obtained by integrating over particle properties, luminosities in various optical and near-infrared bands (ignoring extinction by dust), and mock optical thumbnail images. When referring to a specific galaxy in this work, we specify the unique identifier ('GalaxyID') associated with that galaxy in the public EAGLE data base.

2.2 Galaxy selections

2.2.1 The HRS galaxies

In Section 3 we compare the dust-related properties of EAGLE galaxies with the observed properties of the galaxies in the *Herschel* Reference Survey (HRS, Boselli et al. 2010), and more specifically the subset presented by Cortese et al. (2012).

The HRS consists of a volume-limited sample ($15 \leq D \leq 25$ Mpc) including late-type galaxies with 2MASS (Skrutskie et al. 2006) K-band magnitude $K_S \leq 12$ mag and early-type galaxies with $K_S \leq 8.7$ mag. The total sample consists of 322 galaxies (260 late- and 62 early-type galaxies). As argued by Boselli et al. (2010), this sample is representative of the Local Universe and it spans different density regimes from isolated galaxies to the centre of the Virgo cluster.

The HRS sub-sample analysed by Cortese et al. (2012) includes only those galaxies for which *Herschel* as well as H I, NUV and SDSS observations are available, i.e. a total of 282 galaxies (234 late- and 48 early-type galaxies). As argued by Cortese et al. (2012), the sub-sample is representative of the full HRS sample, and it is thus representative of the local galaxy population as well.

According to Hughes et al. (2013) and Viaene et al. (2016), only 5–8 per cent of the HRS galaxies potentially host an active galactic nucleus (AGN), depending on the criteria used. Furthermore, Viaene et al. (2016) argue that the dust attenuation properties of the potential AGN hosts (and thus their FIR emission) do not differ fundamentally from those of the other galaxies in the sample. Consequently, we do not exclude or single out these galaxies.
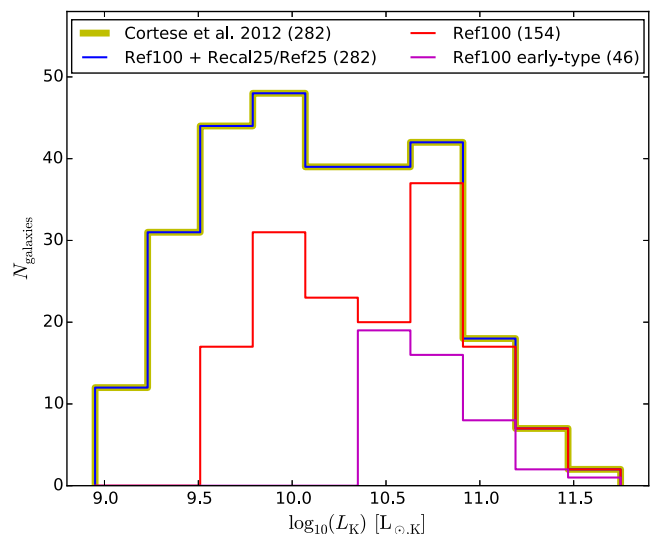

Figure 1. The K-band luminosity distribution of the galaxies in the Cortese et al. (2012) HRS sub-sample (dark yellow) and of the EAGLE galaxies selected for this work (blue) to match that sample. The curves are identical for both of the sets $\mathcal{C}$ and $\mathcal{F}$ listed in Table 2. The distribution of the galaxies taken from the standard-resolution snapshot Ref100 is shown in red; the remainder of the galaxies are taken from one of the higher resolution snapshots, i.e. either Recal25 or Ref25. The distribution of the early-type galaxies, which are all taken from the Ref100 snapshot, is shown in magenta.

2.2.2 Selecting EAGLE galaxies

To enable a proper comparison between our mock observations and the HRS data, we construct a random sample of 282 present-day EAGLE galaxies mimicking the selection criteria described for HRS in Section 2.2.1. Because we have not yet produced any mock observations from which to derive galaxy properties, we use the intrinsic galaxy properties provided in the public EAGLE data base (McAlpine et al. 2016). We first restrict our sample to galaxies with a minimum stellar mass of $10^{9.4}$ $M_\odot$ for galaxies drawn from the Ref100 snapshot, and $10^{8.5}$ $M_\odot$ for galaxies drawn from the Recal25 and Ref25 snapshots. These mass cutoffs ensure a minimum numerical resolution of roughly 2000 stellar particles per galaxy, as can be seen from the initial particle masses in Table 1, taking into account the mass transfer due to feedback processes over the lifetime of the stellar populations represented by the particles. As a consequence, our selection favours the high-resolution snapshots Recal25 or Ref25 for galaxies at the lower end of the mass range.

We then use the galaxy-type-dependent K-band selection criteria described in Section 2.2.1, assuming that all EAGLE galaxies are placed at a distance of 20 Mpc (the median distance of the HRS sample). We employ the sSFR, $\dot{M}_*/M_*$, as a simple proxy for galaxy type, considering galaxies with sSFR $< 10^{-11}$ yr^{-1} to be early-type (see e.g. fig. 8 in the review by Kennicutt & Evans 2012). Finally, we randomly reject galaxies until the sample matches the K-band luminosity distribution of the HRS sub-sample studied by Cortese et al. (2012), as shown in Fig. 1.

In fact, we construct two sets of EAGLE galaxies, named $\mathcal{C}$ and $\mathcal{F}$, that each match these criteria. Table 2 and Fig. 1 illustrate the make-up of these sets. Both sets contain *the same* collection of 154 galaxies drawn from the Ref100 snapshot, including 46 early-type galaxies. In addition, set $\mathcal{C}$ includes 128 galaxies drawn from the Recal25 snapshot, and set $\mathcal{F}$ likewise includes 128 galaxies drawn from the Ref25 snapshot. These two additional subsets have an identical K-band luminosity distribution, and contain no

Table 2. Characteristics of the two sets of EAGLE galaxies for which we present results in this work. The first two columns show a symbol to identify the set and a mnemonic for the origin of this symbol. Subsequent columns list the total number of galaxies in the set and the number of galaxies extracted from each of the EAGLE snapshots used in this work (see Table 1). The final column shows the number of early-type galaxies in each set.

Set	Mmenonic	Total	Ref100	Recal25	Ref25	Early-type
$\mathcal{C}$	ReCal25	282	154	128	–	46
$\mathcal{F}$	ReF25	282	154	–	128	46

early-type galaxies. For the lower luminosity bins, the mix of galaxies drawn from the various snapshots is limited by the lack of low-mass galaxies in the Ref100 snapshot, as indicated earlier. For the higher luminosity bins, the mix is limited by the number of galaxies available for each bin in the smaller volume Recal25 or Ref25 snapshots.

Our analysis in Section 3 is mostly based on set $\mathcal{C}$. However, we evaluate the effects of the recalibration and numerical resolution of the EAGLE simulations by also investigating some of the key results for set $\mathcal{F}$.

2.3 The radiative transfer code SKIRT

SKIRT[1] (Baes et al. 2011; Camps & Baes 2015) is a public multi-purpose 3D Monte Carlo dust radiative transfer code for simulating the effect of dust on radiation in astrophysical systems. It offers full treatment of absorption and multiple anisotropic scattering by the dust, computes the temperature distribution of the dust and the thermal dust re-emission self-consistently, and supports stochastic heating of dust grains (Camps et al. 2015). The code handles multiple dust mixtures and arbitrary 3D geometries for radiation sources and dust populations, including grid- or particle-based representations generated by hydrodynamical simulations. The dust density distribution is discretized using one of the built-in dust grids, including state-of-the art octree (Saftly et al. 2013), *k*d-tree (Saftly, Baes & Camps 2014) and Voronoi (Camps, Baes & Saftly 2013) grids. The wide range of built-in components can be configured to construct complex models in a parameter file or through a user-friendly interface (Baes & Camps 2015; Camps & Baes 2015).

While SKIRT is predominantly used to study dusty galaxies (e.g. Baes & Dejonghe 2002; Baes et al. 2010, 2011; De Looze et al. 2012; De Geyter et al. 2014; Saftly et al. 2015), it has also been applied to active galactic nuclei (Stalevski et al. 2012), molecular clouds (Hendrix, Keppens & Camps 2015), and stellar systems (Deschamps et al. 2015). In this work, we use the SKIRT code to perform dust radiative transfer simulations on selected EAGLE galaxies, producing integral field spectroscopy (IFS) data cubes and spectral energy distributions (SEDs) from UV to submm wavelengths as further described in the following sections.

2.4 Preparing EAGLE galaxies for SKIRT

2.4.1 Extracting galaxies from an EAGLE snapshot

Trayford et al. (in preparation) present a procedure for modelling EAGLE galaxies from optical to near-infrared wavelengths
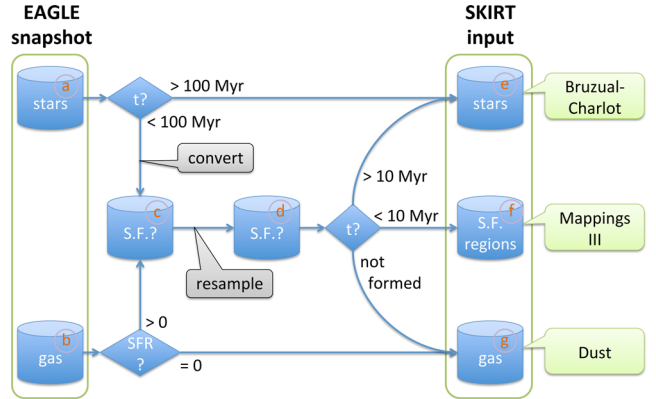
---

[1] SKIRT documentation: http://www.skirt.ugent.be. SKIRT code repository: https://github.com/skirt/skirt.

Figure 2. Schematic overview of the procedure used for preparing EAGLE galaxies for SKIRT. See the text in Section 2.4 for more details.

(0.28–2.5μm) using SKIRT, generating spectra, broad-band photometry, line indices, and multi-band images for a large population of galaxies at redshift $z = 0.1$. We follow the same procedure, paying attention to dust emission and producing spectra and photometry over a much broader wavelength range (0.02–2000μm).

Fig. 2 illustrates the overall process of extracting the data for a galaxy from the EAGLE snapshot and preparing them for post-processing in SKIRT. For our purposes, a galaxy in an EAGLE snapshot is defined as a gravitationally bound substructure in a halo of dark and baryonic matter represented by particles. These structures are identified by the friends-of-friends and SUBFIND (Springel et al. 2001; Dolag et al. 2009) algorithms, which are run on the output of the EAGLE simulations. To study a particular galaxy, we extract the corresponding sets of star particles and gas particles (items *a* and *b* in Fig. 2). Following the convention used by Schaye et al. (2015), any particles outside a spherical aperture with radius of 30 kpc are ignored. The origin of the coordinate system is positioned at the galaxy's stellar centre of mass. Unless noted otherwise, we retain the galaxy's original orientation, resulting in a 'random' viewing angle. In those few cases where we study the results for specific viewing angles, the face-on view looks down from the positive net stellar angular momentum vector of the galaxy, and the edge-on view observes from an arbitrary direction perpendicular to this vector.

2.4.2 Re-sampling star-forming regions

Star formation in EAGLE occurs stochastically: at each time step, a gas particle has a certain probability of being wholly converted to a star particle. Because individual particle masses are rather high (of the order of $10^6 M_\odot$ for the reference simulation, see Table 1), a typical EAGLE galaxy contains only a small number of young star particles, unrealistically clumping all of the galaxy's young stars in a few point-like regions. This introduces sampling issues, which we alleviate by reprocessing the star-forming gas particles and the youngest star particles before feeding them into the SKIRT radiative transfer code, as illustrated in Fig. 2.

As a first step, we build a set of star-forming region candidates (item *c* in Fig. 2), including all star particles younger than 100 Myr – the typical time-scale of a starburst (Groves et al. 2008) – and all gas particles with a non-zero SFR. All other particles, i.e. older star particles and non-star-forming gas particles, are transferred directly to the corresponding SKIRT input sets (items *e* and *g* in Fig. 2). The young star particles are converted back to star-forming gas particles.

The SFR at the time of birth of these particles is calculated using the relation between pressure and SFR described in section 4.3 of Schaye et al. (2015) and originally in Schaye & Dalla Vecchia (2008), which is based on the empirical Kennicutt–Schmidt law (Kennicutt 1998).

In the second step, the star-forming region candidates are re-sampled into a number of sub-particles (item *d* in Fig. 2) with lower masses drawn randomly from the power-law mass distribution function,

$$\frac{dN}{dM} \propto M^{-1.8} \quad \text{with } M \in [700, 10^6]\,\text{M}_\odot. \tag{1}$$

This distribution of masses is inspired by observations of molecular clouds in the Milky Way reported by Heyer, Carpenter & Snell (2001) and reviewed in section 2.5 of Kennicutt & Evans (2012). Once a sufficient number of sub-particles have been generated to approximately represent the parent particle's mass, the sub-particle masses are proportionally adjusted to ensure exact mass conservation. The resulting sub-particles are assigned a formation time sampled randomly to represent their parent's SFR and mass, assuming a constant SFR over a 100 Myr lifetime. The sub-particles that formed less than 10 Myr ago – the typical lifetime of an H II region (Groves et al. 2008) – are placed into a new SKIRT input set defining star-forming regions (item *f*); those that formed more than 10 Myr ago are recast as star particles (item *e*); and those that have not yet formed are recast as gas particles (item *g*).

Finally, the smoothing lengths and positions of the star-forming sub-particles are adjusted to match our post-processing assumptions as explained in Section 2.4.4.

2.4.3 Deriving the diffuse dust distribution

Table 3 offers an overview of the parameters defining the SKIRT radiative transfer model for each type of input particles, as discussed in the current and the following section. We derive a dust mass, M_{dust}, for each particle in SKIRT's 'gas' input set (item *g* in Fig. 2) according to

$$M_{\text{dust}} = \begin{cases} f_{\text{dust}}\, Z\, M & \text{if } T < T_{\text{max}} \text{ or SFR} > 0 \\ 0 & \text{otherwise,} \end{cases} \tag{2}$$

where Z, M, T, and SFR are the metallicity (metal mass fraction),[2] current mass, temperature, and star formation rate given by the gas particle's properties in the EAGLE snapshot, and f_{dust} and T_{max} are free parameters. The characterization of gas particles based on the conditions of equation (2) is illustrated in Fig. 3 for an EAGLE disc galaxy. The star-forming (blue) and cold (cyan) gas particles trace the spiral arms in the galactic disc, while the hot gas (red) is located in the outskirts, as expected.

In summary, equation (2) assumes that a constant fraction f_{dust} of the metallic gas is locked up in dust, as long as the gas is forming stars or the gas is colder than the cutoff temperature T_{max}. The assumption of a fixed dust-to-metal fraction f_{dust} is observed to be an appropriate approximation for a variety of environments (Dwek 1998; James et al. 2002; Brinchmann et al. 2013; Zafar & Watson 2013). We will vary this parameter as part of our analysis in Section 3.

The condition SFR > 0 captures the re-sampled gas particles that are eligible for star formation but were not actually converted into a

---

[2] We use the SPH smoothed metallicity rather than the particle metallicity; see Wiersma et al. (2009b) and Schaye et al. (2015) for more information.

Table 3. Input parameters of the SKIRT radiative transfer model for each type of EAGLE particle, in addition to the particle position. The procedure for deriving a dust distribution from the gas particles (item *g* in Fig. 2) is discussed in Section 2.4.3. The procedures for the particles representing stellar populations and star-forming regions (items *e* and *f* in Fig. 2) are discussed in Section 2.4.4.

| Param	Description	Origin
Dust distribution		
h	Smoothing length	Particle
M	Current gas mass	Particle
Z	Gas metallicity	Particle
T	Temperature of the gas	Particle
SFR	Star formation rate of the gas	Particle
T_{max}	Highest temperature at which gas contains dust	Preset value
f_{dust}	Fraction of the metallic gas locked up in dust	Free param
Young and evolved stars		
h	Smoothing length	Particle
M_{init}	Birth mass of the stellar population	Particle
Z	Metallicity of the stellar population	Particle
t	Age of the stellar population	Particle
Star-forming regions		
h	Smoothing length	Calculated
M	Mass of the H II region	Sampled
SFR	Star formation rate of the H II region	Calculated
Z	Metallicity of the H II region	Parent particle
ρ	Gas density at the H II region's position	Parent particle
P	Pressure of the ambient ISM	Calculated
C	Compactness of the H II region	Calculated
f_{PDR}	Dust covering fraction of the PDR region	Free param
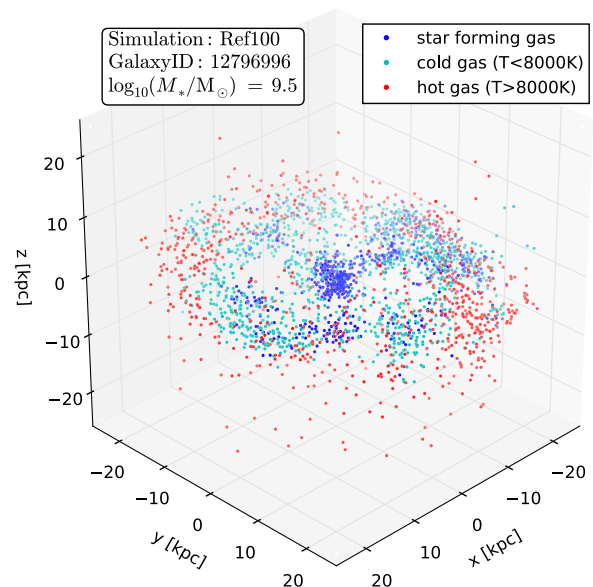
Figure 3. A projection of the gas particle positions in an EAGLE disc galaxy hand-picked for illustrative purposes. Our procedure allocates dust for star-forming gas (blue) and for cold gas (cyan). Hot gas (red) is deemed not to contain any dust.

star-forming region (the 'not formed' arrow between items *d* and *g* in Fig. 2). We need this condition because the EAGLE simulations assign a non-physical temperature to star-forming gas particles (see Section 2.1). However, by definition, the star-forming gas can be assumed to be sufficiently cold to form dust.

The temperature cutoff $T < T_{max}$ for the non-star-forming gas particles accounts for the fact that dust cannot form, or is rapidly destroyed, in hot gas (e.g. Guhathakurta & Draine 1989). We need to determine an appropriate temperature cutoff value. Unfortunately, since the EAGLE simulations do not model the cold gas phase in the ISM (see Section 2.1), we cannot properly constrain T_{max} using a physically motivated procedure. For our analysis in Section 3, we select a value of $T_{max} = 8000$K, corresponding to the value of T_{eos} at $n_H = 0.1$cm^{-1} used in the EAGLE simulations (section 4.3 of Schaye et al. 2015).

2.4.4 Assigning SEDs to particles

Each particle in SKIRT's 'stars' input set (item *e* in Fig. 2) is assigned a stellar population SED from the Bruzual & Charlot (2003) family, using the birth mass, metallicity (see footnote 2) and age given by the particle properties in the EAGLE snapshot (see Table 3 for an overview). We use the low resolution version of the Padova1994/Chabrier model, which is one of the two models recommended by Bruzual & Charlot (2003).

For the particles in the 'star-forming regions' input set (item *f* in Fig. 2) we follow the procedure described by Jonsson et al. (2010). Each particle is assigned an appropriate starburst SED from the MAPPINGS III family (Groves et al. 2008). These templates model both the H II region and the photodissociation region (PDR) surrounding the star-forming core, including the dust contained in those regions. We attempt to compensate for the additional dust mass assumed by the MAPPING III model by removing the equivalent amount of dust from the diffuse dust component. We now discuss this process in more detail.

The MAPPINGS III templates are parametrized by the SFR and the metallicity of the star-forming region, the pressure of the ambient ISM, the H II region compactness, and the covering fraction of the associated PDR (see Table 3 for an overview). The SFR is determined from the mass assigned to the star-forming particle (as discussed in Section 2.4.3), assuming a constant SFR during the H II region's lifetime of 10 Myr (following Groves et al. 2008). The metallicity, Z, is taken directly from the particle properties (see footnote 2) in the EAGLE snapshot. The ambient pressure of the ISM, P, is calculated from the particle's density, ρ, using the polytropic equation of state imposed on star-forming particles (see Section 2.1). The H II region compactness, C, is designed to reflect the dust temperature distribution in the H II region (time-averaged over its lifetime), so that it predominantly controls the form of the FIR continuum dust emission. In our procedure the value of this parameter is derived from the ambient pressure, P, and our assigned particle mass, M (see equation 1), using equation (13) of Groves et al. (2008), i.e.

$$\log_{10} C = \frac{3}{5} \log_{10} \left(\frac{M}{M_\odot} \right) + \frac{2}{5} \log_{10} \left(\frac{P/k_B}{\text{cm}^{-3}\,\text{K}} \right), \quad (3)$$

where k_B is the Boltzmann constant. Finally, the parameter f_{PDR} is defined as the time-averaged dust covering fraction of the PDR surrounding the star-forming core over the H II region's lifetime. Starbursts in which the PDR's dust entirely envelops the H II region have $f_{PDR} = 1$, while uncovered H II region complexes have $f_{PDR} = 0$. The covering fraction is treated as a free parameter, which we will vary as part of our analysis in Section 3.

As indicated above, the MAPPINGS III templates model the dust residing in the PDR region in addition to the core H II region itself. Following Jonsson et al. (2010), we consider the region represented by the MAPPINGS III templates (including PDR and H II region) to

be ten times as massive as the star-forming core represented by the particle. To determine the spatial extent of the region's emission, we assume that the region's centre has the same density as the local ambient ISM. For the cubic spline kernel employed in SKIRT, this leads to the easily inverted relation, $10M = (\pi/8)\rho h^3$, between the H II region mass, M, the ambient density, ρ, and the particle smoothing length, h. We also randomly shift the positions of the star-forming sub-particles within the smoothing sphere of the parent particle (see Section 2.4.2) to avoid overlap between the modelled regions.

To avoid double counting the dust residing in the PDR region, we subtract this PDR dust from the diffuse dust distribution derived as discussed in Section 2.4.3. We insert a 'ghost' gas particle with negative mass in the SKIRT gas input set (see Section 2.4.3) for each star-forming particle. The ghost particle receives the (negative) mass of the corresponding PDR region, i.e. ten times the mass of the star-forming particle. When sampling the gas (or dust) density field, SKIRT combines the negative ghost densities with the positive densities defined by the other particles, clipping the total density to zero if needed. To lower the probability of this occurring, we artificially increase the smoothing length of the ghost particle by a factor of three. According to our tests, this sufficiently alleviates the issue without otherwise affecting the results.

2.5 Radiative transfer on EAGLE galaxies

This section describes the SKIRT configuration used to perform the radiative transfer simulations on the EAGLE galaxies.

2.5.1 Dust grid

The SKIRT radiative transfer procedure requires the dust density distribution of the system under study to be discretized over a dust grid. Within each grid cell, the dust density and all other physical quantities, such as the radiation field, are assumed to be constant. SKIRT implements a performance-optimized mechanism to calculate the dust mass in each grid cell from the smoothed particles defining a galaxy. The particles are interpolated using a scaled and truncated Gaussian kernel designed to approximate a finite-support cubic spline kernel (Altay & Theuns 2013; Baes & Camps 2015).

Here, we use an adaptive, hierarchical Cartesian grid that encloses the 30 kpc aperture considered for each galaxy (see Section 2.4.1). Specifically, we use an octree grid (Saftly et al. 2013) that automatically subdivides cells until each cell contains less than a fraction $\delta_{max} = 3 \times 10^{-6}$ of the total dust mass in the model, with a maximum of 10 subdivision levels (see Fig. 4). The smallest possible cell is thus about 60 pc on a side, which offers 5–10 times better resolution than the typical gravitational softening length in the EAGLE simulations (see Table 1).

Fig. 5 provides some relevant statistics on the discretization of the diffuse dust density for the EAGLE galaxies analysed in this work. The leftmost panel shows that about half of the galaxies in our selection have more than 3000 gas particles that include dust, i.e. particles representing cold or star-forming gas (see Section 2.4.3), which is sufficient to spatially resolve the diffuse dust distribution. Further analysis (not shown) indicates that about 100 of our galaxies have less than 100 'dusty' gas particles, however this includes most of the early-type galaxies, which do not contain much dust anyway.

The two middle panels of Fig. 5 show properties of the dust grids constructed by SKIRT to perform radiative transfer on our EAGLE galaxies. Most dust grids have more than 250 000 cells, which is more than sufficient to resolve the imported smoothed particles.
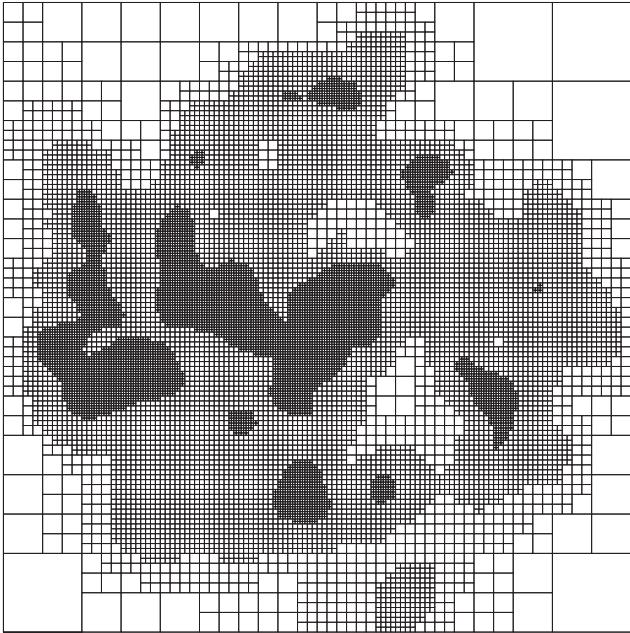
Figure 4. A cut along the galactic plane through an octree dust grid constructed for the EAGLE galaxy shown in Fig. 3. The darker areas trace regions of higher dust density (the grid has smaller dust cells and thus more cell boundaries). For presentation purposes, the illustrated grid uses fewer refinement levels and covers a smaller aperture than the grid actually used by SKIRT in this work (25 kpc radius rather than 30 kpc).

Also, over 90 per cent of the dust cells in each grid have a *V*-band optical depth of less than 0.12 (and most have much lower optical depth), indicating that the grid properly resolves even the densest regions in the dust mass.

The rightmost panel of Fig. 5 shows the difference between the dust mass obtained by summing over all cells in the dust grid, and the dust mass obtained by summing over the incoming particles. For most galaxies, this dust discretization error is limited to less than a third of a per cent, with some outliers of up to 1.5 per cent. While part of this error is caused by grid resolution limitations, further analysis (not shown) indicates that the larger discrepancies in the outliers are caused by the negative dust masses which are introduced to compensate for the dust modelled by star-forming regions (see Section 2.4.4). Specifically, the imported dust density becomes negative in some areas, and is then clipped to zero when building the dust grid.

2.5.2 Dust model

To represent the diffuse dust in the EAGLE galaxies, we use the model presented by Zubko, Dwek & Arendt (2004). This model includes a dust mixture of non-composite graphite and silicate grains and neutral and ionized polycyclic aromatic hydrocarbon (PAH) molecules, designed so that the global dust properties accurately reproduce the extinction, emission and abundance constraints of the Milky Way. The optical properties are taken from Bruce Draine's website[3] (Draine & Lee 1984; Laor & Draine 1993; Li & Draine 2001). The calorimetric properties follow the prescription of Draine & Li (2001). The grain size distributions for each population are taken from Zubko et al. (2004).

---

[3] http://www.astro.princeton.edu/draine/dust/dust.diel.html

The dust emission spectrum is calculated for each dust cell based on the stellar radiation absorbed by the dust in that cell. The calculation includes the effects of stochastically heated grains, i.e. dust grains and PAH molecules that are not in local thermal equilibrium with the radiation field, using the scheme described by Camps et al. (2015). To facilitate this calculation, SKIRT discretizes the size range of the dust grains into several size bins, for each type of grain material separately. For this work, following the recommendations of Camps et al. (2015), SKIRT uses 15 size bins for each of the graphite and silicate components, and 10 size bins for each of the neutral and ionized PAHs.

The MAPPINGS III templates, used in our post-processing procedure to model star-forming regions (Section 2.4.4), employ a dust model with optical properties taken from the same sources (Laor & Draine 1993; Li & Draine 2001). The grain size distribution and the treatment of PAHs (Dopita et al. 2005; Groves et al. 2008) are similar but not identical to our model for the diffuse dust. While we do not believe these differences substantially affect our analysis and conclusions, it is important to note the uncertainties involved with the selection of a dust model.

2.5.3 Wavelength discretization

The SKIRT code employs a single wavelength grid for all calculations. The input SEDs and dust properties are sampled on this grid, photon packages are given wavelengths corresponding to the grid points, dust absorption and re-emission are calculated for the wavelength bins defined by the grid, and the output fluxes are recorded on the same grid.

The wavelength grid used in all SKIRT calculations for this work is illustrated in Fig. 6. It resolves the relevant features in the input SEDs (see Section 2.4.4) and in the emission spectrum of the dust population (see Section 2.5.2). The grid has 450 wavelength points from 0.02 to 2000 μm laid out on a logarithmic scale. The bin widths are 0.04 dex in the outer wavelength ranges where fluxes are low, 0.02 dex in the dust emission continuum, 0.01 dex in the optical range, and under 0.01 dex in the PAH emission range and for specific emission or absorption features in the employed input spectra.

To further inspect this discretization, we compare band-integrated fluxes (see Appendix A) calculated on our default 450-point wavelength grid with those calculated on a high-resolution grid with 20 000 points. For this purpose, we select a typical SED for a stellar population, one for a star-forming region, and one for stochastically heated dust (see Fig. 6). We calculate the fluxes for these SEDs in a set of bands essentially covering the complete wavelength range, using equations (A4) or (A6). The results calculated on our 450-point wavelength grid are accurate to within 0.1 mag for all bands, and often much better. The results for the bands used in this work are listed in Table 4.

2.5.4 Photon packages

The SKIRT radiative transfer simulation proceeds in two phases. In the first phase, SKIRT launches photon packages randomly originating at the stars and the star-forming regions, and traces these packages through the dusty medium. The simulation loop accounts for the effects of scattering off dust grains, and keeps track of the radiation absorbed in each dust cell. After this phase completes, the code calculates the emission spectrum of the dust population in each dust cell based on the established radiation field, taking into account the
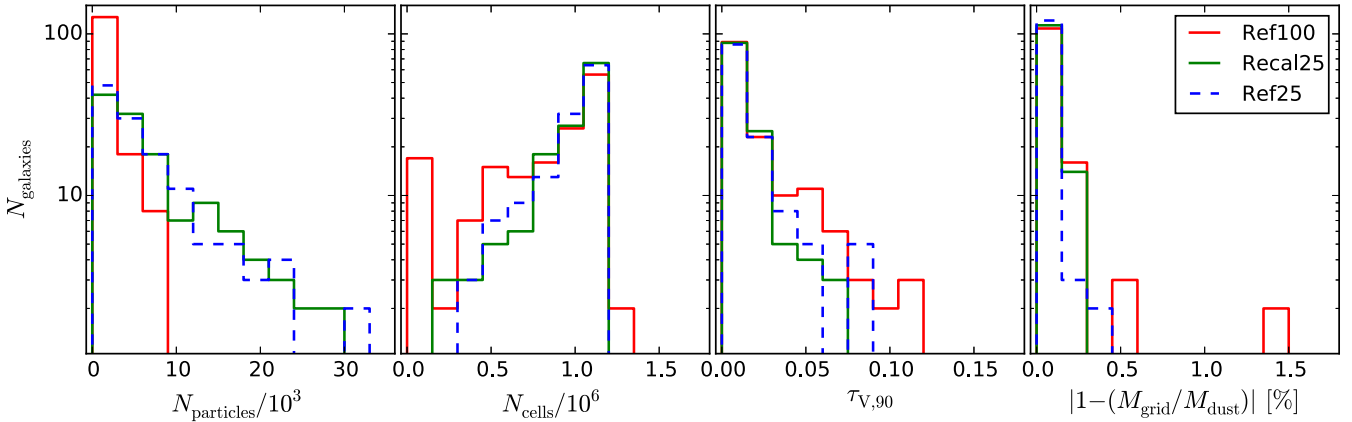
Figure 5. Distribution of SKIRT dust discretization properties for the EAGLE galaxies analysed in this work (see Table 2), processed with $f_{dust} = 0.3$. From left to right: the number of gas particles that include dust (i.e. cold or star-forming gas particles); the number of cells in the dust grid constructed by SKIRT; the 90 per cent percentile V-band optical depth of the cells in the dust grid; the discretization error on the total dust mass (i.e. difference between the dust mass in the grid and in the incoming particles).
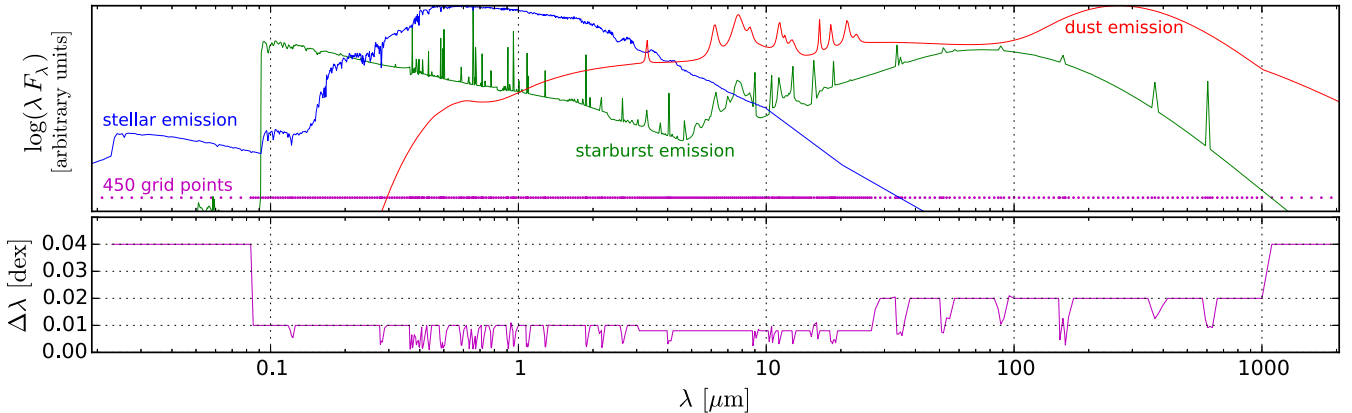
Figure 6. Characteristics of the wavelength grid used in all SKIRT calculations for this work. The three curves in the top panel illustrate typical SEDs for an evolved stellar population (blue), a star-forming region including young stellar objects and dust (green), and stochastically heated diffuse dust (red), plotted on an arbitrary logarithmic scale. The dots (magenta) represent the wavelength grid points. The curve in the bottom panel (magenta) indicates the distance between successive wavelength points on a logarithmic scale.

probabilistic thermal emission of small grains and PAH molecules (Camps et al. 2015). In the second phase, SKIRT launches photon packages originating from the dust distribution, corresponding to the calculated emission spectra, and traces these packages through the dusty medium as well.

For this work, we instruct SKIRT to ignore dust heating by photon packages emitted from the dust, substantially reducing the calculation time. This is justified because the body of dust in a normal galaxy is essentially transparent to infrared radiation. We verified this assumption for our EAGLE sample by comparing the simulation results with and without dust self-heating for the highest dust-mass galaxies. Finally, we configure SKIRT to launch 5×10^5 photon packages for each of the 450 points in the wavelength grid during each of the two phases. Thus the SKIRT simulation for each EAGLE galaxy traces 4.5×10^8 photon packages. In Section 2.5.6 we confirm that this choice is appropriate.

2.5.5 Mock fluxes

Mock detectors are placed along two of the coordinate axes at a fixed distance of 20 Mpc from the model, using parallel projection. If the model has been properly rotated (see Section 2.4.1), this results in a face-on and an edge-on view of the galaxy. The selected

detector distance matches the median distance of the HRS galaxies; see Section 2.2.2. Each detector records an integral field data cube (a 400×400 pixel frame at each of the wavelength grid points) in addition to the spatially integrated fluxes at each wavelength grid point. From these results, we produce band-integrated fluxes and absolute magnitudes corresponding to the following filters (see also Table 4): *GALEX* FUV/NUV (Morrissey et al. 2007); SDSS *ugriz* (Doi et al. 2010); 2MASS *JHK* (Cohen, Wheaton & Megeath 2003); *WISE* W1/W2/W3/W4 (Wright et al. 2010); *Spitzer* MIPS 24/70/160 (Rieke et al. 2004); *Herschel* PACS 70/100/160 (Poglitsch et al. 2010); and *Herschel* SPIRE 250/350/500 for extended sources (Griffin et al. 2010).

To obtain the integrated fluxes, we convolve the simulated SED with the instrument's response curve. The precise procedure depends on whether the instrument counts photons or measures energy (bolometer); the formulae are summarized in Appendix A. The *GALEX*, SDSS, 2MASS and *WISE* instruments are photon counters; the *Spitzer* MIPS and the *Herschel* PACS and SPIRE instruments are bolometers.

Because our analysis in Section 3 relies heavily on the *Herschel* SPIRE 250/350/500 fluxes, and because actual observations in these submm bands suffer from fairly severe observational limitations, we perform an additional procedure for these fluxes. Table 5 lists

Table 4. Evaluation of the wavelength grid and numerical convergence for the SKIRT simulations in this work. The first two columns list the name of the instrument for which mock broad-band fluxes are calculated and the corresponding pivot wavelength according to equations (A5) or (A7). The next three columns show the differences between the magnitude calculated on a high-resolution wavelength grid and on our default wavelength grid, for the three SEDs shown in Fig. 6. The last column shows the maximum magnitude differences for SEDs calculated from SKIRT simulations with different dust grid resolutions and numbers of photons. The horizontal white space separates photon counters (top) and bolometers (bottom).

Band	λ_{pivot} (μm)	Wavelength grid			Dust grid and photons (Δ mag)
		SF region (Δ mag)	Stellar (Δ mag)	Dust (Δ mag)	
GALEX FUV	0.1535	0.002	0.041	–	0.004
GALEX NUV	0.2301	0.003	0.007	–	0.003
SDSS u	0.3557	0.047	0.027	0.001	0.002
SDSS g	0.4702	0.087	0.005	0.001	0.001
SDSS r	0.6176	0.054	0.003	0.001	0.002
SDSS i	0.7490	0.011	0.002	0.002	0.002
SDSS z	0.8947	0.016	0.005	0.001	0.001
2MASS *J*	1.239	0.016	0.014	0.011	0.001
2MASS *H*	1.649	0.011	0.012	0.003	0.002
2MASS K_S	2.164	0.003	0.013	0.002	0.001
WISE W1	3.390	0.021	0.003	0.018	0.001
WISE W2	4.641	0.005	0.005	0.001	0.001
WISE W3	12.57	0.001	0.001	0.001	0.003
WISE W4	22.31	0.001	0.001	0.009	0.003
MIPS 24	23.59	0.001	0.001	0.008	0.003
MIPS 70	70.89	0.001	0.001	0.001	0.003
MIPS 160	155.4	0.001	0.001	0.001	0.004
PACS 70	70.77	0.001	0.001	0.001	0.002
PACS 100	100.8	0.001	0.001	0.001	0.003
PACS 160	161.9	0.001	0.008	0.001	0.004
SPIRE 250 ext	252.5	0.001	–	0.001	0.034
SPIRE 350 ext	354.3	0.001	–	0.001	0.034
SPIRE 500 ext	515.4	0.026	–	0.001	0.035

Table 5. Properties of the *Herschel* SPIRE 250/350/500 instruments used in our mock flux derivation. The beam FWHM and beam area are taken from Ciesla et al. (2012). For the flux limit, we use the confusion noise level from Nguyen et al. (2010).

	Units	250 μm	350 μm	500 μm
Beam FWHM	arcsec	18.2	24.5	36.0
Beam area	arcsec^2	423	751	1587
Flux limit	mJy beam^{-1}	5.8	6.3	6.8

the relevant instrument properties, taken from Ciesla et al. (2012) and Nguyen et al. (2010). We first perform a convolution with the corresponding instrument response function for each of the 400 × 400 pixels in the recorded frames. We then convolve the resulting frame (spatially) with a Gaussian filter scaled to the full width at half-maximum (FWHM) of the instrument's beam, and re-bin the pixels in the frame to match the beam area of the instrument. From this frame, we eliminate all pixels with a flux value below the sensitivity level of the instrument, and we finally sum over the remaining pixels to obtain the total flux.

While the analysis in this work uses spatially integrated fluxes, it is instructive to examine images illustrating the results of our procedures. Fig. 7 shows face-on and edge-on views of a Milky Way-like EAGLE galaxy post-processed as described in this methods section. The images combine an optical view using SDSS *g*, *r* and
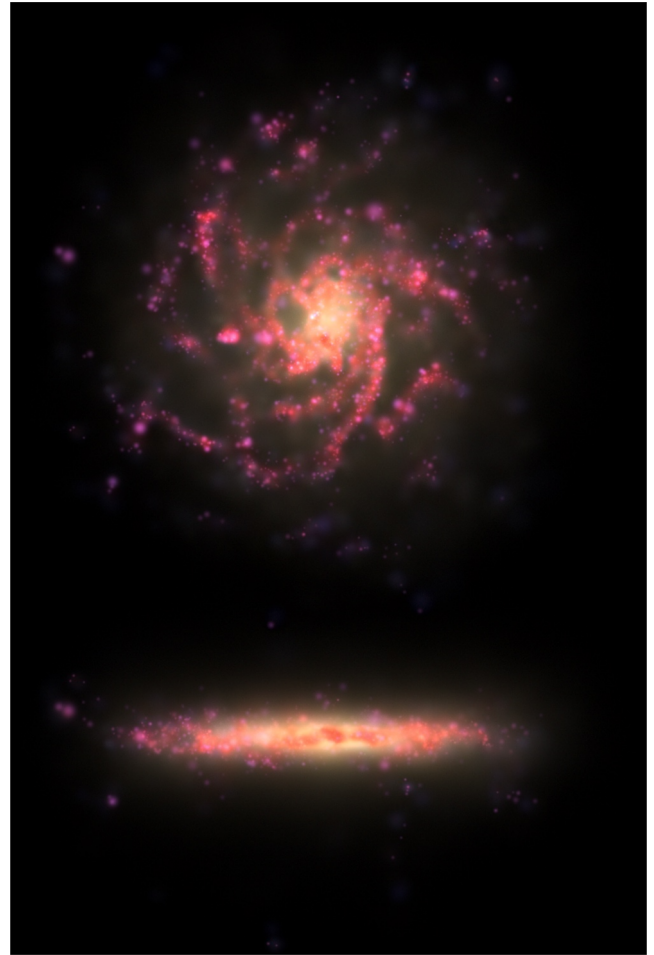

Figure 7. Face-on (top) and edge-on (bottom) views of a Milky Way-like EAGLE galaxy (Ref25; GalaxyID 639646; $M_* = 1.75 \times 10^{10} M_\odot$) post-processed using our procedures. The images combine optical colours (blue, green and red for SDSS *g*, *r* and *i* fluxes) with additional blue for *GALEX* NUV flux and red for *Herschel* PACS 100 μm flux. The views cover an aperture with 30 kpc radius and their orientation is defined by stellar angular momentum, as described in Section 2.4.1.

i fluxes with additional blue for *GALEX* NUV flux and red for *Herschel* PACS 100 μm flux. To obtain these fluxes, the data cubes recorded by SKIRT were convolved, pixel by pixel, with the response curve for each instrument. The resulting purple colours indicate star-forming regions, which strongly emit both in the NUV and FIR. The red colours indicate bodies of diffuse interstellar dust.

2.5.6 Numerical convergence

A numerical convergence test can help ascertain that our discretization settings are appropriate. To this end, we perform the SKIRT simulations for galaxy set $\mathcal{C}$ (Table 2) using a higher resolution dust grid and shooting more photon packages than for our default setup. Specifically, we set the maximum mass fraction per cell to $\delta_{max} = 2 \times 10^{-6}$ rather than 3×10^{-6} (see Section 2.5.1), and we increase the number of photon packages launched per wavelength grid point to 10^6 from 5×10^5 (see Section 2.5.4). We then calculate the fluxes in the various bands used for this work according to the procedure described in Section 2.5.5, and we compare the results from the high-resolution simulation with those from the default setup. The rightmost column in Table 4 shows the absolute value of the
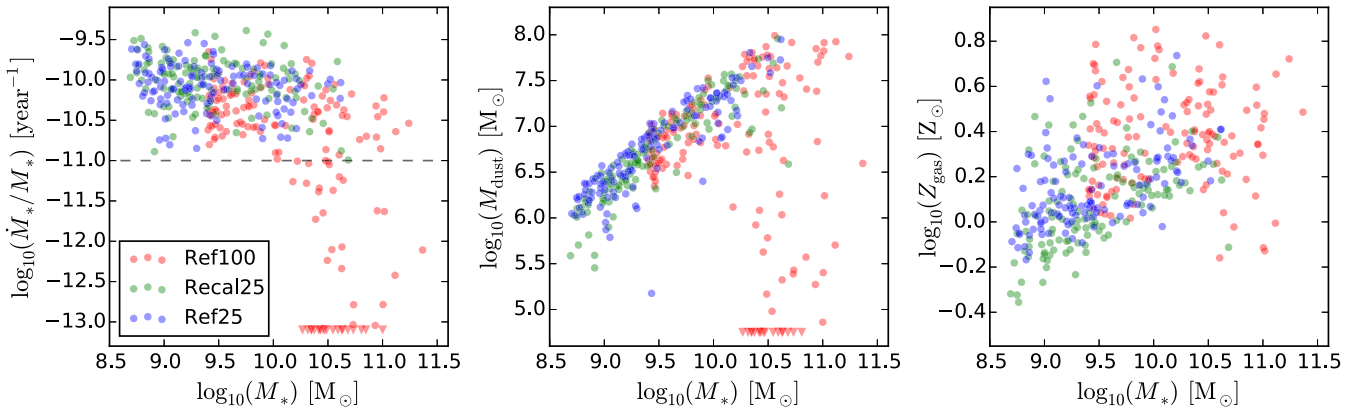
Figure 8. Selected intrinsic properties of the EAGLE galaxies analysed in this work (see Table 2) plotted versus intrinsic stellar mass. Left-hand panel: sSFR; galaxies with sSFR below $10^{-11}\,\mathrm{yr}^{-1}$ (dashed line) are deemed to be early-types; galaxies with sSFR below $10^{-13.1}\,\mathrm{yr}^{-1}$ are plotted as upper bounds at that value. Middle panel: dust mass, assuming a dust-to-metal fraction $f_{\mathrm{dust}} = 0.3$; galaxies with dust mass below $10^{4.75}\,\mathrm{M}_\odot$ are plotted as upper bounds at that value. Right-hand panel: overall metallicity of the gas that includes dust, in units of $Z_\odot = 0.0127$; galaxies with zero dust mass are omitted.

resulting magnitude differences. The fluxes are accurate to within 0.05 mag for all bands, and even to within 0.005 mag for all but the four longest-wavelength bands. The somewhat larger errors for the *Herschel* SPIRE 250/350/500 bands are caused by our implementation of the observational limits in these bands (see Section 2.5.5), which heavily depends on the precise 2D distribution of the fluxes in the simulated images.

Overall, we conclude that the quality of the dust grid and the number of photons in our default setup are sufficient for our purposes.

3 RESULTS AND DISCUSSION

In the following subsections we present results for EAGLE galaxies that were post-processed according to equation (2) with $f_{\mathrm{dust}} = 0.3$ and $f_{\mathrm{PDR}} = 0.1$. We will further justify these parameter values in Section 3.5.

3.1 Intrinsic properties

Although our aim in this work is to evaluate mock observations of the EAGLE galaxies, it is instructive to briefly review some intrinsic properties, even if only to confirm that these values fall in the appropriate range. To this end, Fig. 8 shows selected intrinsic properties of the EAGLE galaxies analysed in this work, i.e. properties that can be calculated from the particles extracted from the snapshot without radiative transfer processing. Consistent with our selection criteria (Fig. 1), most high-mass and all early-type EAGLE galaxies are extracted from the Ref100 snapshot (red points). The remaining galaxies are extracted from the Recal25 snapshot (green points) or from the Ref25 snapshot (blue points) depending on the galaxy set under consideration (Table 2).

The leftmost panel of Fig. 8 plots sSFR versus stellar mass. As in Section 2.2.2, we can use the sSFR as a simple proxy for galaxy type, considering galaxies with a sSFR value below $10^{-11}\,\mathrm{yr}^{-1}$ (indicated by the horizontal dashed line) to be early-type. Comparing this diagram to, e.g. fig. 8 of Kennicutt & Evans (2012), we conclude that both sSFR and stellar mass values are in the expected range, and we can clearly recognize a blue cloud of star-forming galaxies above the dashed line. The red sequence of quiescent galaxies below the dashed line is less prominent because our selection disfavours

these galaxy types to reflect the HRS sample (see Sections 2.2.1 and 2.2.2).

The middle panel of Fig. 8 plots dust mass versus stellar mass. The dust mass is calculated by summing the result of equation (2) over all gas particles, using a dust-to-metal fraction $f_{\mathrm{dust}} = 0.3$. Comparing this figure to, e.g. fig. 16 of Bourne et al. (2012), we conclude that these dust masses are within the expected range. The low dust masses for some of the high-stellar-mass (early-type) galaxies are also consistent with observations (di Serego Alighieri et al. 2013).

The rightmost panel of the same figure plots the metallicity of the gas that contains dust versus stellar mass. The galaxies in our sample have a fairly high metallicity compared to observations (Tremonti et al. 2004; Hughes et al. 2013; Zahid et al. 2014). For example, the metallicities of the HRS galaxies shown in fig. 4 of Hughes et al. (2013) do not exceed $\log_{10}(Z/Z_\odot) = 0.2$, assuming $12 + \log_{10}(\mathrm{O/H})_\odot = 8.69$ (Allende Prieto, Lambert & Asplund 2001). The high metallicities in our sample are, however, consistent with the mass-metallicity relation of the EAGLE galaxies reported in fig. 13 of Schaye et al. (2015). It is noted there that the Ref100 EAGLE simulation systematically over-predicts metallicity in the stellar mass range $M_* < 10^{9.5}\,\mathrm{M}_\odot$. In addition to the uncertainties in both the normalization and the shape of the observed mass–metallicity relation, this discrepancy is most likely caused by the systematic uncertainties in the nucleosynthetic yields adopted in the EAGLE simulations. It is also evident from the right-hand panel of Fig. 8 that galaxies in Recal25 tend to have lower metallicities than galaxies in Ref25, again consistent with the findings of Schaye et al. (2015). Apparently, the stronger outflows in the Recal25 simulation reduce the metallicity of the ISM. Because we use a constant dust-to-metal fraction, see equation (2), this leads to a slightly higher dust content for most Ref25 galaxies (middle panel of Fig. 8).

3.2 Inferred stellar and dust masses

We compare the stellar mass derived from mock observations of our EAGLE galaxies to the intrinsic stellar mass calculated by summing over all stellar particles. We mimic the procedure employed by Cortese et al. (2012), determining the 'mock' stellar mass M_* from the *i*-band luminosity L_i and the $g - i$ colour through

$$\log_{10} \frac{M_*}{\mathrm{M}_\odot} = \log_{10} \frac{L_i}{L_{i,\odot}} + a + b \times (g - i), \qquad (4)$$
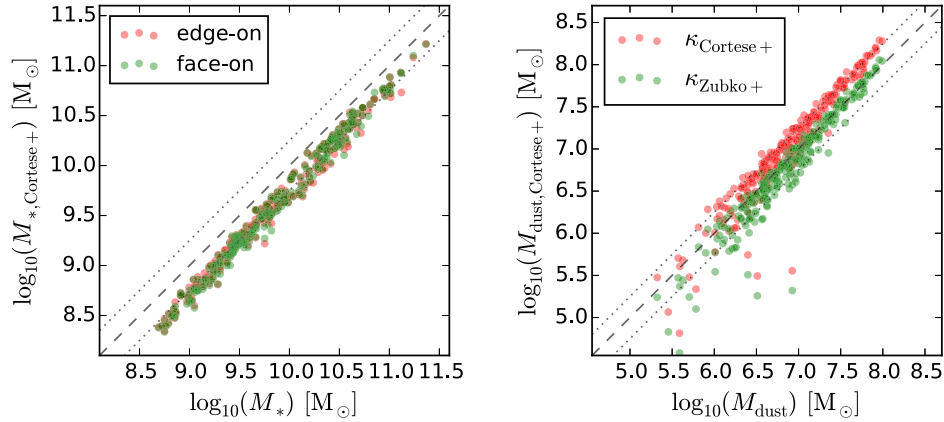
Figure 9. Comparison of stellar and dust mass derived from mock observations of the EAGLE galaxies in set $\mathcal{C}$ (Table 2) with the corresponding intrinsic properties. The EAGLE galaxies were post-processed using $f_{\rm dust} = 0.3$ and $f_{\rm PDR} = 0.1$. The dashed diagonal in each panel indicates the one-to-one relation; the dotted lines indicate ± 0.25 dex offsets. Left-hand panel: stellar mass estimated through equation (4) following Cortese et al. (2012) and Zibetti, Charlot & Rix (2009) using edge-on (red) and face-on fluxes (green). Right-hand panel: dust mass estimated through equation (5) following Cortese et al. (2012) using $\beta = 2$ and the two values of κ_{350} defined in the text; galaxies with dust mass below $10^{4.75}\,{\rm M_\odot}$ are omitted.

with coefficients $a = -0.963$ and $b = 1.032$ taken from table B1 of Zibetti et al. (2009). The result is shown in the left-hand panel of Fig. 9. The mock observations of our EAGLE galaxies underestimate the stellar mass by about 0.25 dex, for both edge-on and face-on fluxes. The Zibetti et al. (2009) recipe assumes the Chabrier (2003) initial mass function (IMF), as do the EAGLE simulations (see section 4.3 of Schaye et al. 2015) and the SED templates we assign to stellar particles (see our Section 2.4.4 and section 2.3 of Bruzual & Charlot 2003), so there is no need to compensate for offsets between different IMFs in the model. However, the Zibetti et al. (2009) calibration of the stellar mass-to-light ratio relation was derived for resolved parts of galaxies. Several authors have proposed different values for the coefficients a and b (e.g. Gallazzi & Bell 2009; Taylor et al. 2010, 2011; Baldry et al. 2012), resulting in a systematic shift of up to 0.3 dex in the relation. In the following sections, we use the Zibetti et al. (2009) calibration because we will be confronting the mock observations with the results presented by Cortese et al. (2012).

We now compare the dust mass derived from mock observations with the dust mass calculated by summing over all gas particles according to equation (2). Following Cortese et al. (2012) and many other authors, the flux f_ν emitted by a modified blackbody at the frequency ν can be written as

$$f_\nu = \frac{M_{\rm dust}}{d^2} \kappa_\nu B_\nu(T_{\rm dust}) \qquad \text{with} \quad \kappa_\nu = \kappa_{350} \left(\frac{\nu}{\nu_{350}} \right)^\beta, \tag{5}$$

where $M_{\rm dust}$ is the dust mass, d is the distance, $B_\nu(T)$ is the Planck function, $T_{\rm dust}$ is the dust temperature, κ_ν is the dust mass absorption coefficient, assumed to depend on frequency through a power law with index β, and κ_{350} is the dust mass absorption coefficient at a wavelength of 350 μm. Cortese et al. (2012) use the values $\beta = 2$ and $\kappa_{350} = \kappa_{\rm Cortese+} = 0.192\,{\rm m^2\,kg^{-1}}$. The Zubko et al. (2004) dust model used in this work (see Section 2.5.2) has the same power-law index, $\beta = 2$. However, the absorption coefficient $\kappa_{350} = \kappa_{\rm Zubko+} = 0.330\,{\rm m^2\,kg^{-1}}$ differs substantially, causing a shift of 0.24 dex in the inferred dust mass.

Cortese et al. (2012) use the three *Herschel* SPIRE 250/350/500 fluxes to estimate the dust mass, employing a recipe presented in their appendix B. The right-hand panel of Fig. 9 plots the dust mass estimates calculated from SKIRT fluxes for our EAGLE galaxies according to this recipe, using $\beta = 2$ and the two values of κ_{350}

defined in the previous paragraph. When using $\kappa_{350} = \kappa_{\rm Cortese+}$, the Cortese et al. (2012) recipe overestimates the dust mass. With the $\kappa_{350} = \kappa_{\rm Zubko+}$ appropriate for our dust model, however, the estimates are fairly accurate, although there is significant scatter in the low mass range. Because we will be confronting our mock observations with the results presented by Cortese et al. (2012), we use their dust mass recipe with $\kappa_{350} = \kappa_{\rm Cortese+}$ in the following sections.

3.3 Inferred SFRs

We compare in Fig. 10 three of the SFR indicators listed in table 1 of Kennicutt & Evans (2012), calculated for mock observations of our EAGLE galaxies, to the intrinsic SFR provided in the public EAGLE data base (McAlpine et al. 2016). The leftmost panel of Fig. 10 shows the SFR based on the *GALEX* NUV flux (Hao et al. 2011; Murphy et al. 2011) using edge-on (red) and face-on fluxes (green). At these short wavelengths, the edge-on fluxes suffer significantly more from dust extinction than the face-on fluxes, especially in more active galaxies, and thus yield a correspondingly lower SFR. However, even the indicator based on face-on fluxes slightly underestimates the SFR for most galaxies. For a small number of outliers, mostly in the lower SFR regime, the indicator substantially overestimates the SFR. These outliers are passive galaxies with a low dust content (the edge-on and face-on fluxes are equal so there is little extinction), where the NUV radiation emitted by the evolved star population is interpreted as a sign of star formation by the indicator. This so-called UV-upturn is also found in observations (e.g. Brown et al. 1997, 2003).

The middle panel of Fig. 10 shows the SFR based on the integrated total infrared flux (3–1100 μm; Hao et al. 2011; Murphy et al. 2011). Because dust is mostly transparent to radiation at these wavelengths, the emission is isotropic and there is no need to compare edge-on and face-on fluxes. This indicator is fairly accurate, except for a number of outliers mostly in the lower SFR regime. In these cases, the emission from diffuse dust residing in the outskirts of those galaxies is interpreted by the indicator as a sign of star formation, while the dust is in fact being heated by an evolved star population. This phenomenon is also found in observations (Bendo et al. 2015).
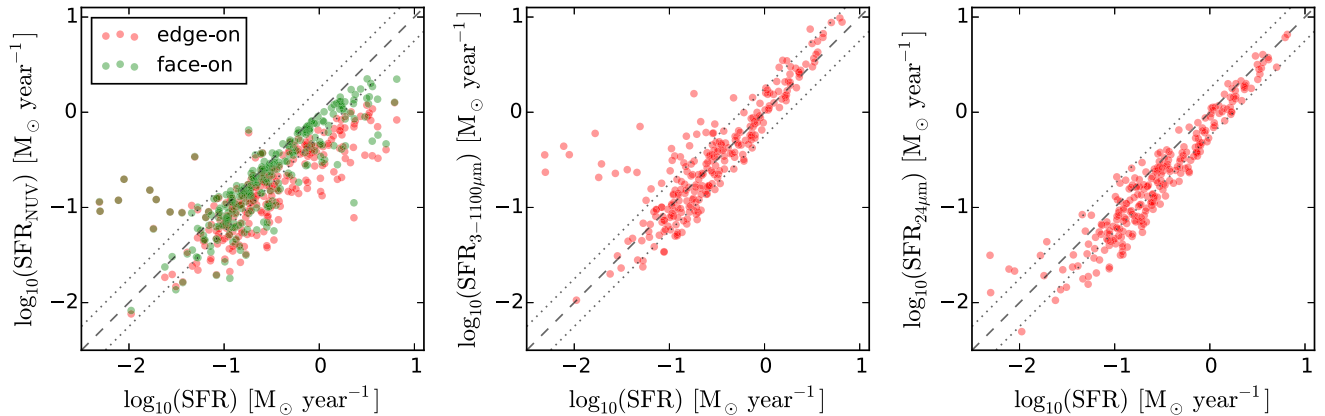
Figure 10. Comparison of three of the SFR indicators summarized in table 1 of Kennicutt & Evans (2012), calculated for mock observations of the EAGLE galaxies in set $\mathcal{C}$ (Table 2), to the intrinsic SFR provided in the public EAGLE data base (McAlpine et al. 2016). The EAGLE galaxies were post-processed using $f_{dust} = 0.3$ and $f_{PDR} = 0.1$. The dashed diagonal in each panel indicates the one-to-one relation; the dotted lines indicate ± 0.25 dex offsets. Left-hand panel: SFR based on *GALEX* NUV flux (Hao et al. 2011; Murphy et al. 2011) using edge-on (red) and face-on fluxes (green). Middle panel: SFR based on integrated 3–1100 μm flux (Hao et al. 2011; Murphy et al. 2011). Right-hand panel: SFR based on *Spitzer* MIPS 24 μm flux (Rieke et al. 2009). In all panels, galaxies with intrinsic or inferred SFR below $10^{-2.5}$ M$_\odot$ year^{-1} are omitted.

The rightmost panel of Fig. 10 shows the SFR based on the *Spitzer* MIPS 24 μm flux (Rieke et al. 2009). Except at the lowest SFRs, this indicator consistently underestimates the intrinsic SFR of our galaxies, which can be understood as follows. The EAGLE simulations do not model the cold ISM phase, and the adjustments made by our post-processing procedure have limitations as well. For example, our model contains isotropically emitting star-forming regions that may not represent the strong variations in the radiation field near star-forming regions sufficiently or accurately. As a consequence, at least some fraction of the diffuse dust in the simulated galaxies is heated insufficiently, resulting in a 24 μm flux lower than observed. In addition, the flux in this wavelength range is very sensitive to the precise properties of the dust, and thus, the dust model used for the simulations (Fanciullo et al. 2015). For example, if the dust grain population contains a larger fraction of small grains, more grains will be stochastically heated to higher energy levels, shifting some of the dust emission to shorter wavelengths and into the 24 μm band, while the total infrared flux remains unchanged.

3.4 Dust scaling relations

In Fig. 11, left-hand panel, we compare mock observations of our EAGLE galaxies (red points) to HRS observations taken from Boselli et al. (2012) and Ciesla et al. (2012) (black points) for a submm colour–colour relation involving the SPIRE fluxes f_{250}, f_{350}, and f_{500}. These fluxes characterize the downwards slope of the dust continuum emission, and thus are sensitive to the cold dust contents. Smaller flux ratios f_{250}/f_{350} and f_{350}/f_{500} indicate a flatter slope of the dust emission curve and thus a larger contribution from colder dust. This is illustrated in the figure by the magenta curve, which traces the flux ratio relation for the emission of a modified blackbody (MBB, see equation 5) with $\beta = 2$ (the value assumed by the dust model used in this work) for temperatures ranging from 13 K to 28 K. Data points away from this curve indicate contributions from dust at various temperatures, resulting in a superposition of MBB curves and thus a broader dust continuum emission peak.

The EAGLE and HRS scaling relations show similar slopes. However, the EAGLE flux ratios are generally smaller than the corresponding HRS flux ratios, i.e. the simulated points are shifted to the area of the plot indicating lower dust temperatures. The

EAGLE galaxies thus show a larger contribution from very cold dust ($T \lesssim 18$ K), confirming our finding in Section 3.3 that part of the simulated dust is insufficiently heated, plausibly because of limitations in the sub-grid models of the simulations. It appears that, even with the sub-grid techniques in our procedures, our model does not fully capture the clumpiness of the dust distribution in galaxies, so that an insufficient amount of dust is irradiated by the strong radiation fields present within and near star-forming regions.

The EAGLE outliers to the right of the MBB curve are caused by the simulated observational limitations built into our procedure. This can be understood by noting that the observational limitations are more severe for longer wavelengths, and furthermore depend on the absolute flux level and its spatial distribution across the sky, so that the effect on the observed flux ratios is strongly non-linear. In fact, in a version of the plot (not shown) using convolved but unlimited submm fluxes, i.e. skipping the operations described in the last paragraph of Section 2.5.5, the EAGLE outliers move to the left of the MBB curve. We may thus surmise that the outlying HRS data points to the right of the MBB curve are similarly caused by observational limitations. The two labeled outliers, IC3718 and M86, are close to the SPIRE detection limit (Boselli et al. 2010; Gomez et al. 2010), supporting this assumption.

To help elucidate the contribution of the star-forming regions to the dust emission from the EAGLE galaxies, the green annotations in the left-hand panel of Fig. 11 indicate the submm flux ratios of the MAPPINGS III templates used to model these regions for a range of input parameter values (see Table 3). The effective dust temperature of an isolated MAPPINGS III star-forming region is mostly determined by the specified metallicity, Z, and compactness, C. The other parameters, including the covering fraction, f_{PDR}, and the ambient pressure, P, have a much smaller impact. The higher-than-observed EAGLE metallicities may thus contribute to the lower dust temperatures. At the same time, the temperature increases rapidly with the H II region's compactness. In fact, the temperature range $T \gtrsim 22$ K is reached only for the highest C values supported by the MAPPINGS III templates. The compactness in turn increases with the H II region mass (see equation 3). We sample these masses for our star-forming regions from a power-law distribution in the range $M \in [10^{2.8}, 10^6]$ M$_\odot$ (see equation 1), while Groves et al. (2008) quote a range of $M \in [10^{3.5}, 10^7]$ M$_\odot$, almost an order of magnitude higher.
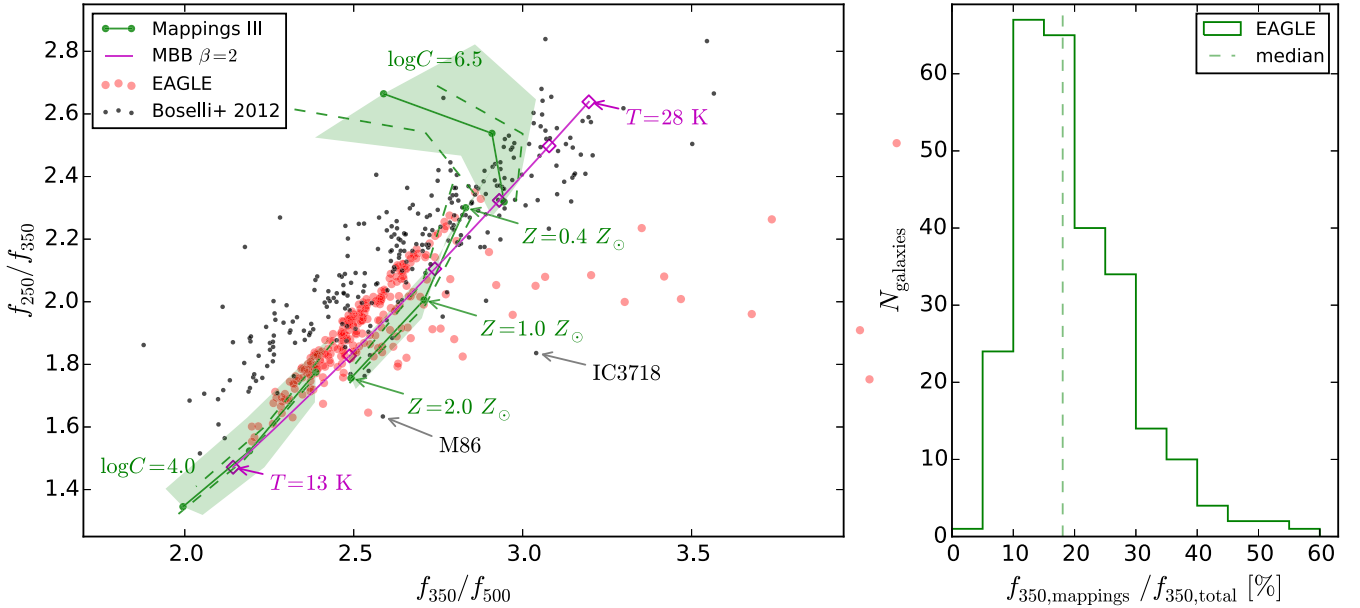
Figure 11. Left-hand panel: *Herschel* SPIRE colour–colour relation f_{250}/f_{350} versus f_{350}/f_{500} for EAGLE galaxies (red points) from set $\mathcal{C}$ (Table 2) compared to HRS observations (black points) taken from Boselli et al. (2012) and Ciesla et al. (2012). The EAGLE galaxies were post-processed using $f_{dust} = 0.3$ and $f_{PDR} = 0.1$. Galaxies for which one or more SPIRE fluxes are below the detection limit are omitted. The magenta curve traces a modified blackbody (MBB) with $\beta = 2$ for temperatures ranging from 13 K to 28 K; the diamonds are spaced by 3 K. The green annotations indicate the flux ratios of the MAPPINGS III templates used to model star-forming regions for a range of input parameter values (see Table 3). The solid lines show ratios for fixed $f_{PDR} = 0.1$ and for the extreme compactness values supported by the templates ($\log_{10} C = 4.0, 6.5$) plus an intermediate value ($\log_{10} C = 5.25$). The dots on the solid lines show the ratios for varying metallicity ($Z = 0.4, 1, 2 \times Z_{\odot}$) with the given compactness. The dashed lines indicate the variation resulting from adjusting f_{PDR} to values of 0.05 (higher temperature) or 0.15 (lower temperature). The shaded areas indicate the variation resulting from adjusting the ambient pressure to the extreme values supported by the templates. Right-hand panel: histogram of the MAPPINGS III contribution to the total flux at 350 μm for the EAGLE galaxies shown in the left-hand panel. The vertical dashed line indicates the median.

Our lower masses, and thus lower C values, might contribute to the apparent lack of warmer dust in our simulated results. These effects are limited, however, because for most galaxies the contribution of the MAPPINGS III templates to the total flux in the submm range is less than 25 per cent, as shown in the right-hand panel of Fig. 11.

In Fig. 12 we compare the dust scaling relations for mock observations of our EAGLE galaxies (red points) to HRS observations taken from Cortese et al. (2012) (black points). In order to make the comparison as unbiased as possible, rather than employing intrinsic properties obtained by summing over the smoothed particles, all EAGLE data points in Fig. 12 are derived from mock observations based on the SEDs generated by SKIRT. Specifically, the stellar masses and dust masses are obtained following the recipes employed by Cortese et al. (2012) and summarized in Section 3.2. Galaxies for which one or more SPIRE fluxes are below the detection limit are plotted as filled triangles rather than circles. For the simulated galaxies, these non-detections are plotted at a fixed value of $M_{dust}/M_* = 10^{-4}$.

The dust-to-stellar mass ratio versus stellar mass scaling relation (left-hand panel of Fig. 12) is reproduced well, including the turn-off above $M_* = 10^{10} \, \mathrm{M}_{\odot}$, although there is a slight positive offset in the dust-to-stellar mass ratio. The relation of dust-to-stellar mass ratio versus NUV − r colour (right-hand panel of Fig. 12) is also reproduced well, including the turn-off. As noted by Cortese et al. (2012), the dust-to-stellar mass ratio anti-correlates strongly with stellar mass and with NUV − r colour, a proxy for sSFR (e.g. Schiminovich et al. 2007). The relations are remarkably similar to the scaling relation involving the H I-to-stellar mass ratio (Catinella et al. 2010; Cortese et al. 2011; Fabello et al. 2011), suggesting that the dust and atomic hydrogen content of galaxies might be directly linked.

These results show that our EAGLE galaxies can indeed reproduce observed scaling relations based on FIR and submm fluxes. In the next section, we will present a quantitative measure for the correspondence between the simulations and data, and we will investigate the effect of changing the parameter values in our post-processing procedure.

3.5 Parameter study

To quantify the correspondence between two sets of data points, such as the mock observations and the HRS data for one of the scaling relations shown in Figs 11 and 12, we use a generalization of the well-known Kolmogorov–Smirnov test (K–S test; Kolmogorov 1933; Smirnov 1948) to two-dimensional distributions. This generalization is due to Peacock (1983) and Fasano & Franceschini (1987), and its detailed implementation is described by Press et al. (2007). The 2D K–S test computes a metric D which can be interpreted as a measure of the 'distance' between two sets of two-dimensional data points, with smaller D values indicating better correspondence.

Figs 13 and 14 illustrate the effect of varying one of the post-processing parameters (respectively f_{dust} and f_{PDR}) on the scaling relations of Figs 11 and 12, i.e. relations between submm flux colours in column (a), dust-to-stellar mass ratio versus stellar mass in column (b), and dust-to-stellar mass ratio versus NUV − r colour in column (c). Each panel in these figures shows the K–S test D value quantifying the discrepancy between the mock observations plotted in that panel and the underlying HRS data points. Because each column shows a particular scaling relation, D values are comparable across the rows within each column, but not between columns.
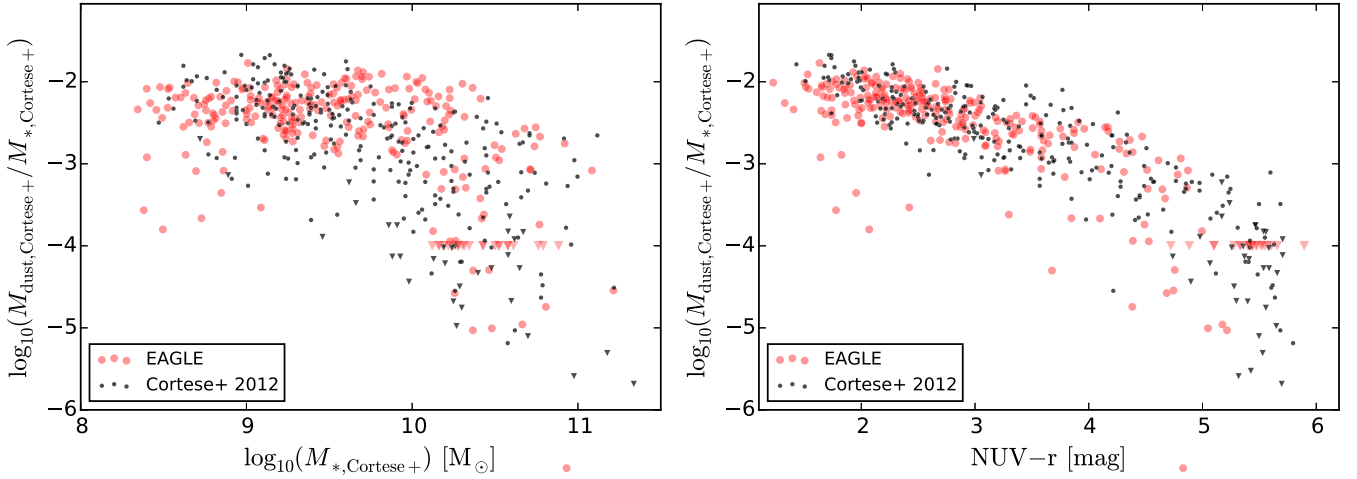
Figure 12. Dust scaling relations for EAGLE galaxies (red points) from set $\mathcal{C}$ (Table 2) compared to HRS observations (black points) taken from Cortese et al. (2012). The EAGLE galaxies were post-processed using $f_{\rm dust} = 0.3$ and $f_{\rm PDR} = 0.1$, and all EAGLE data points are obtained through mock observations (see text). The left-hand panel shows the dust-to-stellar mass ratio versus stellar mass. The right-hand panel shows the dust-to-stellar mass ratio versus $NUV - r$ colour. In both panels, galaxies for which one or more SPIRE fluxes are below the detection limit are plotted as filled triangles rather than circles. For the simulated galaxies, these non-detections are plotted at an arbitrary value of $M_{\rm dust}/M_* = 10^{-4}$.
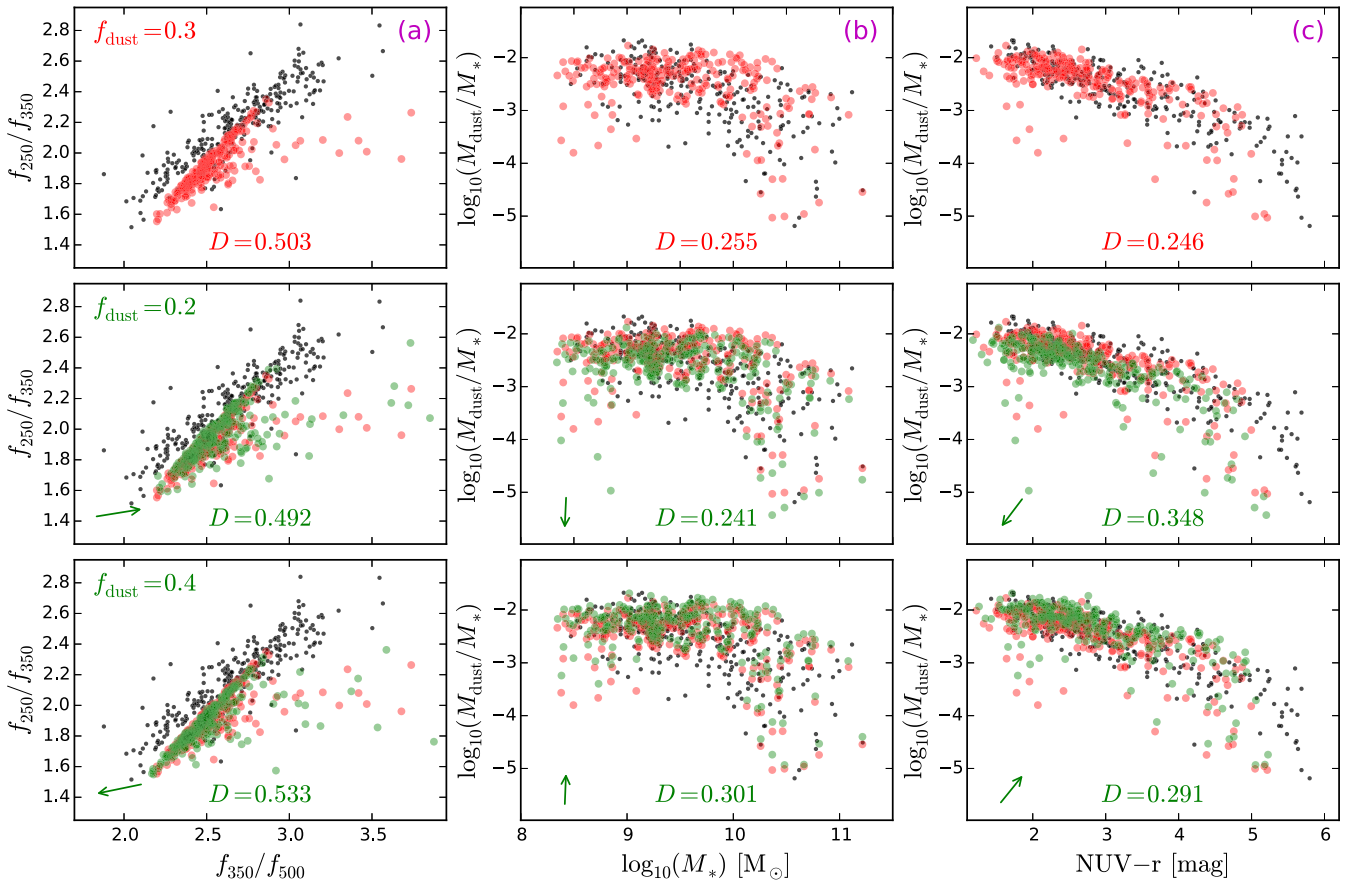
Figure 13. The scaling relations of Fig. 11, shown in column (a), and Fig. 12, shown in columns (b) and (c), for three values of the post-processing parameter $f_{\rm dust}$ (shown across the rows) with a fixed $f_{\rm PDR} = 0.1$. The mock observations (red and green points) are overplotted on the HRS observations (black points) as before. The top row corresponds to the parameter settings of Figs 11 and 12, i.e. $f_{\rm dust} = 0.3$. These red points are repeated in the other rows for reference; the overplotted green points represent the mock observations with $f_{\rm dust} = 0.2$ (middle row) and $f_{\rm dust} = 0.4$ (bottom row). The green arrow in the lower left corner of these panels points in the direction of the average shift from red to green points (the length of the arrow is fixed). The D value is a measure for the correspondence between the mock and HRS observations (smaller is better). Galaxies for which one or more SPIRE fluxes are below the detection limit are omitted from this figure and from the calculation of D.
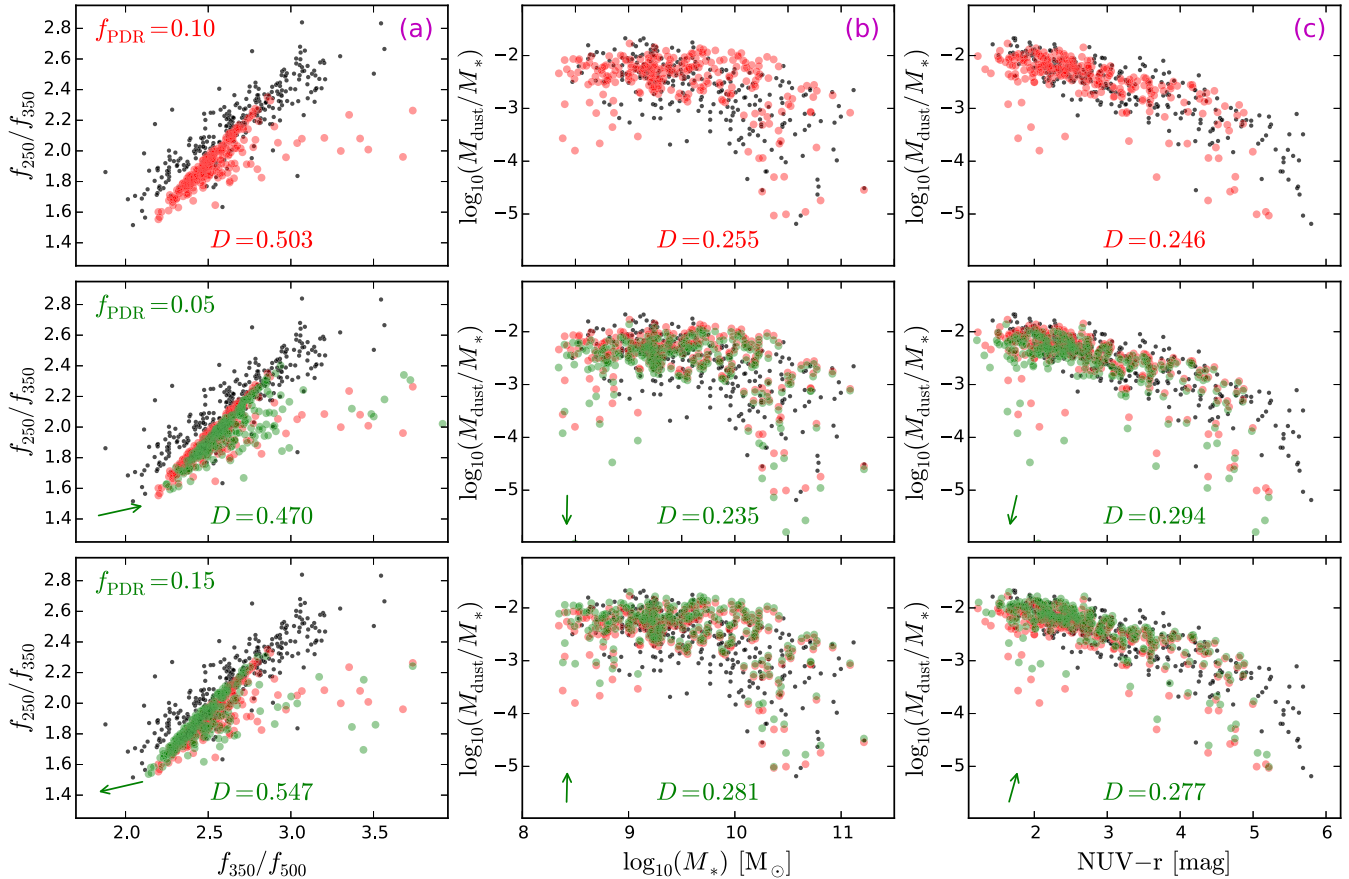
Figure 14. As Fig. 13, but now varying the post-processing parameter f_{PDR} with a fixed $f_{dust} = 0.3$. The top row again corresponds to the parameter settings of Figs 11 and 12, i.e. $f_{PDR} = 0.1$. The overplotted green points in the other rows represent the mock observations with $f_{PDR} = 0.05$ (middle row) and $f_{PDR} = 0.15$ (bottom row).

Fig. 13 illustrates the effect of varying the dust-to-metal fraction f_{dust}. According to equation (2), the diffuse dust mass in a simulated galaxy scales linearly with f_{dust} (the star-forming regions model a separate body of dust that is independent of f_{dust}, see Section 2.4.4). In columns (b) and (c) we indeed see that, with increasing dust-to-metal fraction, the 'observed' dust-to-stellar mass ratio increases, and, for many galaxies, the NUV − r colour shifts redwards because of the extinction caused by the extra dust. Also, as expected, there is very little effect on the 'observed' stellar mass. The effect on the submm colours shown in column (a) is not pronounced, although there seems to be a slight shift towards flatter slopes, i.e. colder dust temperatures, with increasing f_{dust}. This is because the larger body of diffuse dust is heated by the same stellar radiation to a lower average temperature.

Fig. 14 illustrates the effect of varying the covering fraction f_{PDR} of the PDRs modelled in our simulations by the MAPPINGS III templates (see Section 2.4.4). In column (a) we see a shift towards flatter slopes, i.e. colder dust temperatures, with increasing f_{PDR}, caused by the more dispersed obscuration of the star-forming cores by the dust in the PDRs. In columns (b) and (c) we see an effect on the 'observed' dust mass similar to the effect of varying the dust-to-metal fraction (Fig. 13). This effect is caused by the additional dust emission modelled by the MAPPINGS III SEDs for increasing covering fractions. For example, it is clear from the top panel of fig. 6 in Groves et al. (2008) that the continuum dust emission increases in addition to shifting to longer wavelengths. The apparent dust mass derived from a modified blackbody fitted to a MAPPINGS III SED

increases by more than 80 per cent when f_{PDR} changes from 0.05 to 0.1, and by about another 50 per cent when f_{PDR} changes from 0.1 to 0.15, for fixed values of the other parameters (the precise percentages depend on the metallicity and other properties of the PDR). Varying the PDR covering fraction has only a small effect on the NUV − r colour because the dust mass is added in compact regions and does not contribute much to the overall extinction. In fact, in our simulations, the dust in the PDR regions does not contribute at all to the extinction of radiation originating outside of the PDR region, because each region is handled individually using a MAPPINGS III model.

While adjusting f_{dust} or f_{PDR} produces clear overall trends in these scaling relations, the effect varies substantially between individual galaxies, as is especially noticeable for some of the outliers. These differences are caused by varying degrees of extinction by diffuse dust and different levels of contribution from star-forming regions. Also, our emulation of the observational limitations, including instrument resolution and sensitivity, cause a non-linear response of the 'measured' flux to the actual submm emission of an EAGLE galaxy. This is especially true for galaxies with lower dust masses and thus less submm emission.

We used the D value of the Cortese et al. (2012) scaling relation in column (c) of Figs 13 and 14 to determine our standard set of post-processing parameter values, even though the D value for the scaling relations in the other columns can be slightly more optimal for somewhat smaller amounts of dust (i.e. lower values of f_{dust} or f_{PDR}). This leads to adopted values of $f_{dust} = 0.3$, fully compatible
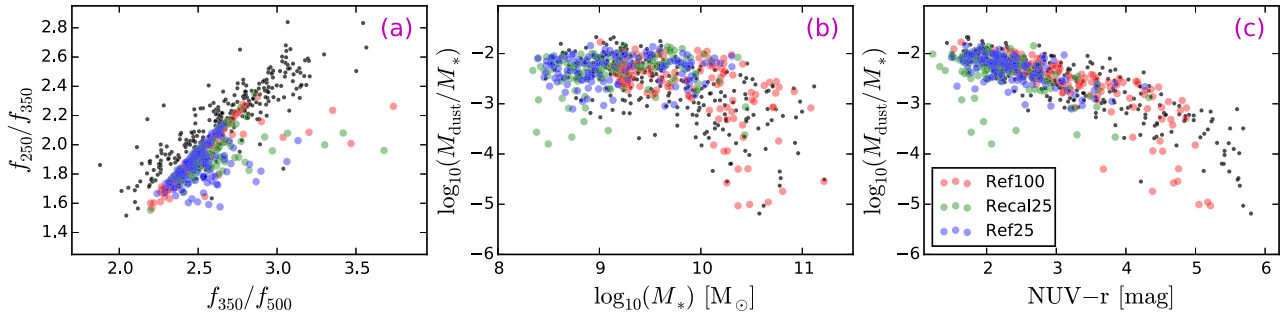
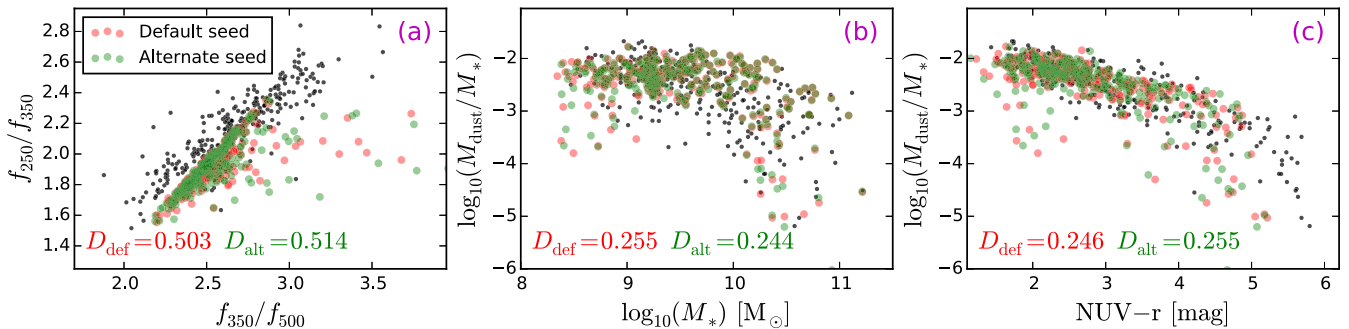**Figure 15.** The scaling relations of Fig. 11, shown in panel (a), and Fig. 12, shown in panels (b) and (c), for all galaxies in sets $\mathcal{C}$ and $\mathcal{F}$ (see Table 2). The points for our galaxies from snapshot Ref25 (blue) are plotted on top of those from Ref100 (red) and Recal25 (green) and the HRS observations (black). As in Figs 11 and 12, the EAGLE galaxies were post-processed using $f_{dust} = 0.3$ and $f_{PDR} = 0.1$. Galaxies for which one or more SPIRE fluxes are below the detection limit are omitted from this plot.

Figure 16. The scaling relations of Fig. 11, shown in panel (a), and Fig. 12, shown in panels (b) and (c), for the galaxies in set $\mathcal{C}$ using $f_{dust} = 0.3$ and $f_{PDR} = 0.1$. The star-forming regions are re-sampled with the default (red) and an alternate (green) pseudo-random sequence to evaluate the effect of these random variations on the SKIRT input model. The D value is a measure for the correspondence between the mock and HRS observations (smaller is better). Galaxies for which one or more SPIRE fluxes are below the detection limit are omitted from this plot.

with the observed range of dust-to-metal fractions from 0.2 to 0.4 (Dwek 1998; Brinchmann et al. 2013; Zafar & Watson 2013), and $f_{PDR} = 0.1$, which is lower than the fiducial value of 0.2 used by Jonsson et al. (2010). It is worth noting once more in this context that the dust masses derived from our mock observations scale inversely with the assumed value of κ_{350} (see Section 3.2). Using κ_{Zubko+} instead of $\kappa_{Cortese+}$ would cause a 0.24 dex downward shift on the vertical axis in columns (b) and (c) of Figs 13 and 14. Adjusting our post-processing parameters to compensate for this shift would evidently affect the absolute dust masses assigned to our galaxies, without, however, changing the actual extinction levels.

We now briefly review the mock observations shown in Fig. 15 for the galaxies extracted from the Ref25 snapshot (part of set $\mathcal{F}$, see Table 1). Based on the rightmost panel of Fig. 8, we already noted in Section 3.1 that the Ref25 galaxies on average have a higher metallicity than the Recal25 galaxies, resulting in a larger dust mass. This effect is evident in columns (b) and (c) of Fig. 15, where the Ref25 galaxies (blue points) are positioned slightly higher, on average, compared to the Recal25 galaxies (green points). Overall the convergence between the lower resolution Ref100 snapshot and the higher resolution Ref/Recal25 snapshots is very good.

For the analysis presented so far, the star-forming region re-sampling procedure described in Section 2.4.2 was performed only once for each galaxy. In other words, for a given galaxy, exactly the same particle input sets were presented to SKIRT for all radiative transfer simulations of that galaxy. This approach has enabled us to focus on the effects of varying the values of f_{dust} and f_{PDR} in the radiative transfer model without interference from random changes in the input model. To verify that no biases were introduced by

our specific instantiation of the star-forming regions, we reran the re-sampling procedure with a different pseudo-random sequence (i.e. a different seed). Fig. 16 shows the calculated scaling relations, using our standard values of $f_{dust} = 0.3$ and $f_{PDR} = 0.1$, for the default and alternate input models. While individual galaxies can differ substantially, especially the outliers, the overall results and conclusions remain unchanged.

4 CONCLUSIONS

We calculated mock observations in the wavelength range from UV to submm for simulated galaxies extracted from the EAGLE suite of cosmological simulations using the radiative transfer code SKIRT. To help overcome some of the resolution limitations of the simulations, we employed sub-grid models for the star-forming regions and for the diffuse dust distribution. We also took special care to mimic the effects of instrumental properties and observational limitations when calculating band-integrated fluxes, which are important especially in submm bands.

To validate our method, and at the same time confront the properties of the simulated galaxies with observed galaxies, we selected a set of present-day EAGLE galaxies that matches the *K*-band luminosity distribution and overall morphological type classification (using the sSFR as a proxy) of the galaxies in the *Herschel* Reference Survey (HRS), a volume-limited sample of about 300 normal galaxies in the Local Universe. We evaluated some intrinsic properties of our selected galaxies (Fig. 8), calculated by summing over the particles, and confirmed that the stellar masses, SFRs and dust

masses fall in the expected range, while the average gas metallicities are above the metallicities observed in comparable galaxies.

We evaluated some relevant tracers by comparing the values derived from our mock observations to the corresponding intrinsic values (Figs 9 and 10). We found that the Zibetti et al. (2009) calibration of stellar mass versus *g*- and *i*-band luminosity used by Cortese et al. (2012) underestimates stellar mass by about 0.25 dex, in line with the systematic uncertainty on the stellar mass-to-light ratio relation reported by other authors. Furthermore, the Cortese et al. (2012) recipe for deriving dust mass from the three SPIRE fluxes produces an offset that seems to be mostly caused by differences in the assumed dust absorption coefficient at 350 μm. The star formation indicators based on, respectively NUV, 24 μm, and integrated infrared fluxes perform fairly well, although the 24 μm estimates are consistently low, most likely because some of the dust in our model is too cold.

We then studied dust scaling relations, including the f_{250}/f_{350} versus f_{350}/f_{500} submm colour-colour relation (Fig. 11) and the dust-to-stellar mass ratio versus stellar mass and versus NUV − *r* colour relations (Fig. 12), comparing the properties derived from mock observations of the EAGLE galaxies with those observed for HRS galaxies. Using our 'standard' set of post-processing parameter values, we found good correspondence between the EAGLE and HRS scaling relations, with one important caveat. The submm colours indicate that the average temperature of the dust in our EAGLE galaxy models is lower than observed. We concluded that, even with the sub-grid techniques in our procedures, our model does not fully capture the clumpiness of the dust distribution in galaxies, so that an insufficient amount of dust is irradiated by the strong radiation fields present within and near star-forming regions.

We investigated the effects of varying the assumed dust-to-metal fraction, f_{dust} (Fig. 13), and PDR covering fraction, f_{PDR} (Fig. 14), in our post-processing procedure. The first parameter controls the diffuse dust, while the latter controls the dust near young stellar populations. We found that the effects on the scaling relations are consistent with expectations, although it is hard to determine unambiguously optimal values for both parameters because of the partial degeneracy of the effects. We settled on $f_{dust} = 0.3$ and $f_{PDR} = 0.1$ as our standard values, noting that these values also depend on the properties of the dust in our model. These parameter values are compatible with observed values of f_{dust} (Dwek 1998; Brinchmann et al. 2013; Zafar & Watson 2013) and values of f_{PDR} suggested by other authors (Jonsson et al. 2010).

In conclusion, our analysis has shown that, in spite of some limitations, the EAGLE simulations can reproduce infrared and submm observations through a physically motivated post-processing procedure. Furthermore, we have used the mock submm observations to constrain the important dust-related parameters in our method, leading to a consistent calculation of dust attenuation in the UV and optical domain by Trayford et al. (in preparation). While we studied present-day galaxies in this work, our post-processing method is equally applicable to galaxies at higher redshifts, and could be readily adapted to other hydrodynamical simulations.

The method presented here opens many opportunities for future work. We plan to add infrared and submm fluxes for a large subset of the EAGLE galaxies at various redshifts to the public EAGLE data base (McAlpine et al. 2016) as a service to other researchers. We could study the morphology and structure of mock EAGLE galaxy images in various wavelength bands from UV to submm, comparing those properties with resolved observations in the same bands. It would also be instructive to post-process some of the more resolved galaxies in the zoom-in simulations (Op-

penheimer et al. 2016; Sawala et al. 2016) based on the EAGLE code.

In a more distant future, the astrophysical community will undoubtedly develop more advanced simulation techniques. Future simulations of galaxy evolution and assembly may use sub-grid recipes on a smaller scale to model a cold phase in the ISM, which will allow more accurate modelling of the clumpy dust structure during post-processing. Radiative transfer codes may include sub-grid models of star-forming regions that are connected to the overall RT model in a self-consistent manner, as opposed to employing 'disconnected' SED templates. We hope that our current work will help inform such future efforts.

REFERENCES

Allende Prieto C., Lambert D. L., Asplund M., 2001, ApJ, 556, L63
Altay G., Theuns T., 2013, MNRAS, 434, 748
Baes M., Camps P., 2015, Astron. Comput., 12, 33
Baes M., Dejonghe H., 2002, MNRAS, 335, 441
Baes M. et al., 2010, A&A, 518, L39
Baes M., Verstappen J., De Looze I., Fritz J., Saftly W., Vidal Pérez E., Stalevski M., Valcke S., 2011, ApJS, 196, 22
Bahé Y. M. et al., 2016, MNRAS, 456, 1115
Baldry I. K. et al., 2012, MNRAS, 421, 621
Bendo G. J. et al., 2015, MNRAS, 448, 135
Boselli A. et al., 2010, PASP, 122, 261
Boselli A. et al., 2012, A&A, 540, A54
Bourne N. et al., 2012, MNRAS, 421, 3027
Brinchmann J., Charlot S., Kauffmann G., Heckman T., White S. D. M., Tremonti C., 2013, MNRAS, 432, 2112
Brown T. M., Ferguson H. C., Davidsen A. F., Dorman B., 1997, ApJ, 482, 685
Brown T. M., Ferguson H. C., Smith E., Bowers C. W., Kimble R. A., Renzini A., Rich R. M., 2003, ApJ, 584, L69
Bruzual G., Charlot S., 2003, MNRAS, 344, 1000
Byun Y. I., Freeman K. C., Kylafis N. D., 1994, ApJ, 432, 114
Camps P., Baes M., 2015, Astron. Comput., 9, 20
Camps P., Baes M., Saftly W., 2013, A&A, 560, A35
Camps P. et al., 2015, A&A, 580, A87
Catinella B. et al., 2010, MNRAS, 403, 683
Chabrier G., 2003, ApJ, 586, L133
Ciesla L. et al., 2012, A&A, 543, A161
Cohen M., Wheaton W. A., Megeath S. T., 2003, AJ, 126, 1090
Cortese L., Catinella B., Boissier S., Boselli A., Heinis S., 2011, MNRAS, 415, 1797

Cortese L. et al., 2012, A&A, 540, A52
Crain R. A. et al., 2015, MNRAS, 450, 1937
Dalla Vecchia C., Schaye J., 2012, MNRAS, 426, 140
De Geyter G., Baes M., Camps P., Fritz J., De Looze I., Hughes T. M., Viaene S., Gentile G., 2014, MNRAS, 441, 869
De Looze I., Baes M., Fritz J., Verstappen J., 2012, MNRAS, 419, 895
Deschamps R., Braun K., Jorissen A., Siess L., Baes M., Camps P., 2015, A&A, 577, A55
di Serego Alighieri S. et al., 2013, A&A, 552, A8
Disney M., Davies J., Phillipps S., 1989, MNRAS, 239, 939
Doi M. et al., 2010, AJ, 139, 1628
Dolag K., Borgani S., Murante G., Springel V., 2009, MNRAS, 399, 497
Domínguez-Tenreiro R., Obreja A., Granato G. L., Schurer A., Alpresa P., Silva L., Brook C. B., Serna A., 2014, MNRAS, 439, 3868
Dopita M. A. et al., 2005, ApJ, 619, 755
Draine B. T., Lee H. M., 1984, ApJ, 285, 89
Draine B. T., Li A., 2001, ApJ, 551, 807
Dwek E., 1998, ApJ, 501, 643
Fabello S., Catinella B., Giovanelli R., Kauffmann G., Haynes M. P., Heckman T. M., Schiminovich D., 2011, MNRAS, 411, 993
Fanciullo L., Guillet V., Aniano G., Jones A. P., Ysard N., Miville-Deschênes M.-A., Boulanger F., Köhler M., 2015, A&A, 580, A136
Fasano G., Franceschini A., 1987, MNRAS, 225, 155
Furlong M. et al., 2015, MNRAS, 450, 4486
Gallazzi A., Bell E. F., 2009, ApJS, 185, 253
Gomez H. L. et al., 2010, A&A, 518, L45
Griffin M. J. et al., 2010, A&A, 518, L3
Groves B., Dopita M. A., Sutherland R. S., Kewley L. J., Fischera J., Leitherer C., Brandl B., van Breugel W., 2008, ApJS, 176, 438
Guhathakurta P., Draine B. T., 1989, ApJ, 345, 230
Guidi G., Scannapieco C., Walcher C. J., 2015, MNRAS, 454, 2381
Haardt F., Madau P., 2001, in Neumann D. M., Tran J. T. V., eds, Clusters of Galaxies and the High Redshift Universe Observed in X-rays, Recent results of XMM-Newton and Chandra, XXXVIth Rencontres de Moriond, XXIst Moriond Astrophysics Meeting, Savoie, France
Hao C.-N., Kennicutt R. C., Johnson B. D., Calzetti D., Dale D. A., Moustakas J., 2011, ApJ, 741, 124
Hayward C. C., Smith D. J. B., 2015, MNRAS, 446, 1512
Hayward C. C., Kereš D., Jonsson P., Narayanan D., Cox T. J., Hernquist L., 2011, ApJ, 743, 159
Hayward C. C., Jonsson P., Kereš D., Magnelli B., Hernquist L., Cox T. J., 2012, MNRAS, 424, 951
Hayward C. C., Narayanan D., Kereš D., Jonsson P., Hopkins P. F., Cox T. J., Hernquist L., 2013, MNRAS, 428, 2529
Hayward C. C. et al., 2014, MNRAS, 445, 1598
Hendrix T., Keppens R., Camps P., 2015, A&A, 575, A110
Heyer M. H., Carpenter J. M., Snell R. L., 2001, ApJ, 551, 852
Hopkins P. F., Kereš D., Oñorbe J., Faucher-Giguère C.-A., Quataert E., Murray N., Bullock J. S., 2014, MNRAS, 445, 581
Hughes T. M., Cortese L., Boselli A., Gavazzi G., Davies J. I., 2013, A&A, 550, A115
James A., Dunne L., Eales S., Edmunds M. G., 2002, MNRAS, 335, 753
Jonsson P., Groves B. A., Cox T. J., 2010, MNRAS, 403, 17
Kennicutt R. C., Evans N. J., 2012, ARA&A, 50, 531
Kennicutt R. C., Jr, 1998, ApJ, 498, 541
Kolmogorov A. N., 1933, G. Ist. Italiano degli Attuari, 4, 83
Laor A., Draine B. T., 1993, ApJ, 402, 441
Le Brun A. M. C., McCarthy I. G., Schaye J., Ponman T. J., 2014, MNRAS, 441, 1270
Li A., Draine B. T., 2001, ApJ, 554, 778
McAlpine S. et al., 2016, Astron. Comput., 15, 72
McKinnon R., Torrey P., Vogelsberger M., 2016, MNRAS, 457, 3775
Morrissey P. et al., 2007, ApJS, 173, 682
Murphy E. J. et al., 2011, ApJ, 737, 67
Narayanan D., Hayward C. C., Cox T. J., Hernquist L., Jonsson P., Younger J. D., Groves B., 2010a, MNRAS, 401, 1613
Narayanan D. et al., 2010b, MNRAS, 407, 1701

Nguyen H. T. et al., 2010, A&A, 518, L5
Oppenheimer B. D. et al., 2016, MNRAS,
Peacock J. A., 1983, MNRAS, 202, 615
Poglitsch A. et al., 2010, A&A, 518, L2
Press W. H., Teukolsky S. A., Vetterling W. T., Flannery B. P., 2007, Numerical Recipes in C++: the Art of Scientific Computing, 3rd edn. Cambridge Univ. Press, Cambridge
Rieke G. H. et al., 2004, ApJS, 154, 25
Rieke G. H., Alonso-Herrero A., Weiner B. J., Pérez-González P. G., Blaylock M., Donley J. L., Marcillac D., 2009, ApJ, 692, 556
Robitaille T. P., Churchwell E., Benjamin R. A., Whitney B. A., Wood K., Babler B. L., Meade M. R., 2012, A&A, 545, A39
Rosas-Guevara Y. M. et al., 2015, MNRAS, 454, 1038
Saftly W., Camps P., Baes M., Gordon K. D., Vandewoude S., Rahimi A., Stalevski M., 2013, A&A, 554, A10
Saftly W., Baes M., Camps P., 2014, A&A, 561, A77
Saftly W., Baes M., De Geyter G., Camps P., Renaud F., Guedes J., De Looze I., 2015, A&A, 576, A31
Sawala T. et al., 2016, MNRAS, 457, 1931
Scannapieco C., Gadotti D. A., Jonsson P., White S. D. M., 2010, MNRAS, 407, L41
Schaller M., Dalla Vecchia C., Schaye J., Bower R. G., Theuns T., Crain R. A., Furlong M., McCarthy I. G., 2015, MNRAS, 454, 2277
Schaye J., 2004, ApJ, 609, 667
Schaye J., Dalla Vecchia C., 2008, MNRAS, 383, 1210
Schaye J. et al., 2010, MNRAS, 402, 1536
Schaye J. et al., 2015, MNRAS, 446, 521
Schiminovich D. et al., 2007, ApJS, 173, 315
Skrutskie M. F. et al., 2006, AJ, 131, 1163
Smirnov N., 1948, Ann. Math. Statist., 19, 279
Springel V., 2005, MNRAS, 364, 1105
Springel V., White S. D. M., Tormen G., Kauffmann G., 2001, MNRAS, 328, 726
Springel V., Di Matteo T., Hernquist L., 2005, MNRAS, 361, 776
Stalevski M., Fritz J., Baes M., Nakos T., Popović L. Č., 2012, MNRAS, 420, 2756
Steinacker J., Baes M., Gordon K. D., 2013, ARA&A, 51, 63
Taylor E. N., Franx M., Glazebrook K., Brinchmann J., van der Wel A., van Dokkum P. G., 2010, ApJ, 720, 723
Taylor E. N. et al., 2011, MNRAS, 418, 1587
Tokunaga A. T., Vacca W. D., 2005, PASP, 117, 1459
Torrey P. et al., 2015, MNRAS, 447, 2753
Trayford J. W. et al., 2015, MNRAS, 452, 2879
Tremonti C. A. et al., 2004, ApJ, 613, 898
Viaene S. et al., 2016, A&A, 586, A13
Vogelsberger M. et al., 2014, MNRAS, 444, 1518
Wang L., Dutton A. A., Stinson G. S., Macciò A. V., Penzo C., Kang X., Keller B. W., Wadsley J., 2015, MNRAS, 454, 83
Whitney B. A., 2011, Bull. Astron. Soc. India, 39, 101
Wiersma R. P. C., Schaye J., Smith B. D., 2009a, MNRAS, 393, 99
Wiersma R. P. C., Schaye J., Theuns T., Dalla Vecchia C., Tornatore L., 2009b, MNRAS, 399, 574
Wright E. L. et al., 2010, AJ, 140, 1868
Zafar T., Watson D., 2013, A&A, 560, A26
Zahid H. J., Dima G. I., Kudritzki R.-P., Kewley L. J., Geller M. J., Hwang H. S., Silverman J. D., Kashino D., 2014, ApJ, 791, 130
Zibetti S., Charlot S., Rix H.-W., 2009, MNRAS, 400, 1181
Zubko V., Dwek E., Arendt R. G., 2004, ApJS, 152, 211

APPENDIX A: SIMULATED BROAD-BAND PHOTOMETRY

This appendix summarizes the formulae used to convolve a simulated SED with an actual instrument's response curve to obtain a band-integrated flux. We essentially follow the treatments given on

Ivan K. Baldry's web page[4] and in the appendix of Tokunaga & Vacca (2005). The procedure depends on whether the instrument counts photons or measures energy.

A1 Photon counters

For a photon counting detector, the number of photons detected per unit time, t, and per unit area, S, from a source with an intrinsic spectral energy distribution $F_\lambda(\lambda)$, or equivalently $F_\nu(\nu)$, by a photon counter with total system response $R(\lambda)$, or $R(\nu)$, can be written as

$$\frac{dN_p}{dt\,dS} = \int \frac{\lambda}{hc} F_\lambda(\lambda) R(\lambda)\,d\lambda = \int \frac{1}{h\nu} F_\nu(\nu) R(\nu)\,d\nu. \quad (A1)$$

We define the source's mean intrinsic flux $\langle F_\lambda \rangle$ and $\langle F_\nu \rangle$ through

$$\frac{dN_p}{dt\,dS} = \langle F_\lambda \rangle \int \frac{\lambda}{hc} R(\lambda)\,d\lambda = \langle F_\nu \rangle \int \frac{1}{h\nu} R(\nu)\,d\nu, \quad (A2)$$

and we define the pivot wavelength λ_{pivot} and frequency ν_{pivot} connecting these two flux representations through

$$\langle F_\nu \rangle = \langle F_\lambda \rangle \frac{\lambda_{\text{pivot}}^2}{c} \quad \text{and} \quad \langle F_\lambda \rangle = \langle F_\nu \rangle \frac{\nu_{\text{pivot}}^2}{c}. \quad (A3)$$

Combining equations (A1) and (A2) yields

$$\langle F_\lambda \rangle = \frac{\int \lambda F_\lambda(\lambda) R(\lambda)\,d\lambda}{\int \lambda R(\lambda)\,d\lambda} \quad \text{and} \quad \langle F_\nu \rangle = \frac{\int F_\nu(\nu) R(\nu)\,d\nu/\nu}{\int R(\nu)\,d\nu/\nu}. \quad (A4)$$

Substituting $d\nu/\nu = d\lambda/\lambda$ in equation (A2) and combining with equation (A3) yields

$$\lambda_{\text{pivot}} = \sqrt{\frac{\int \lambda R(\lambda)\,d\lambda}{\int R(\lambda)\,d\lambda/\lambda}} \quad \text{and} \quad \nu_{\text{pivot}} = \sqrt{\frac{\int R(\nu)\,d\nu/\nu}{\int R(\nu)\,d\nu/\nu^3}}. \quad (A5)$$

A2 Bolometers

For an energy measuring device, the quantities $\lambda R(\lambda)/hc$ and $R(\nu)/h\nu$ in the above analysis must be replaced by the total system transmission $T(\lambda)$ or $T(\nu)$. Equations (A4) and (A5) then become

$$\langle F_\lambda \rangle = \frac{\int F_\lambda(\lambda) T(\lambda)\,d\lambda}{\int T(\lambda)\,d\lambda} \quad \text{and} \quad \langle F_\nu \rangle = \frac{\int F_\nu(\nu) T(\nu)\,d\nu}{\int T(\nu)\,d\nu} \quad (A6)$$

and

$$\lambda_{\text{pivot}} = \sqrt{\frac{\int T(\lambda)\,d\lambda}{\int T(\lambda)\,d\lambda/\lambda^2}} \quad \text{and} \quad \nu_{\text{pivot}} = \sqrt{\frac{\int T(\nu)\,d\nu}{\int T(\nu)\,d\nu/\nu^2}}. \quad (A7)$$

---

[4] http://www.astro.ljmu.ac.uk/ikb/research/mags-fluxes/

This paper has been typeset from a TEX/LATEX file prepared by the author.